Andean Mountain Building and Foreland Basin Evolution During Thin- and Thick-Skinned Neogene Deformation (32–33°S)

Chelsea Mackaman-Lofland[1] , Brian K. Horton[1,2] , Facundo Fuentes[3], Kurt N. Constenius[4], Richard A. Ketcham[1] , Tomas N. Capaldi[1], Daniel F. Stockli[1] , Jean-Baptiste Ammirati[5], Patricia Alvarado[6], and Paola Orozco[6]

[1]Department of Geological Sciences, Jackson School of Geosciences, University of Texas at Austin, Austin, TX, USA, [2]Institute for Geophysics, Jackson School of Geosciences, University of Texas at Austin, Austin, TX, USA, [3]YPF, Buenos Aires, Argentina, [4]Department of Geosciences, University of Arizona, Tucson, AZ, USA, [5]Departamento de Geología, Universidad de Chile, Santiago, Chile, [6]Departamento de Geofísica y Astronomía, Universidad Nacional de San Juan, San Juan, Argentina

Abstract The southern Central Andes recorded retroarc shortening, basin evolution, and magmatic arc migration during Neogene changes in subduction. At 31–33°S, above the modern flat-slab segment, spatial and temporal linkages between thin- and thick-skinned foreland shortening, basement-involved exhumation of the main Cordillera, and lower-crustal hinterland thickening remain poorly resolved. We integrate new geochronological and thermochronological data for thrust sheets and Neogene foreland basin fill with structural, sedimentological, and passive seismic results to reconstruct the exhumation history and evaluate potential geometric linkages across structural domains. $^{40}Ar/^{39}Ar$ ages for volcanic horizons and zircon U-Pb ages for synorogenic clastic deposits in the Manantiales Basin constrain the minimum duration of synorogenic sedimentation to ~22–14 Ma. Detrital zircon age distributions record sequential unroofing of hinterland thrust sheets until ~15 Ma, followed by eastward (cratonward) advance of the deformation front, shutoff of western sediment sources, and a shift from fluvial to alluvial fan deposition at ~14 Ma. Apatite (U-Th)/He cooling ages confirm rapid exhumation of basement-involved structural blocks and basin partitioning by ~14–5 Ma, consistent with the timing of the Manantiales facies and provenance shifts and a coeval (~12–9 Ma) pulse of thin-skinned shortening and exhumation previously identified in the eastern foreland. Late Miocene–Pliocene (~8–2 Ma) cooling ages along the Chile-Argentina border point to hinterland uplift during the latest stage of Andean orogenesis. Finally, geophysical constraints on crustal architecture and low-temperature thermochronometry results are compatible with a hybrid thin- and thick-skinned décollement spanning retroarc domains.

1. Introduction

Cordilleran mountain building is the product of shortening, magmatism, and crustal thickening along a subduction margin (e.g., Dewey, 1980; Isacks, 1988; Schellart, 2017). However, the processes and interactions that influence crustal deformation, thickening of the overriding plate, topographic uplift, and synorogenic basin evolution remain poorly understood. Retroarc fold-thrust belts provide important constraints on the geometry, kinematics, and magnitude of crustal shortening and thickening due to structural repetition (Farías et al., 2010; Giambiagi et al., 2012; Ramos et al., 2004). Synorogenic deposits further record shortening-related exhumation, thrust loading, sediment redistribution, and the development of topographic barriers across the orogen (DeCelles, 2012; DeCelles & Giles, 1996; Horton, 2018a; Jordan, 1995). With sufficient spatial and temporal constraints, retroarc fold-thrust belt and foreland basin systems provide nearly continuous, quantitative records of deformation, erosion, and subsidence that are fundamental to understanding the growth and evolution of subduction-related orogens (e.g., Anderson et al., 2017; Horton, 2018b; Kley, 1996; Kley & Monaldi, 1998; McQuarrie, 2002).

The southern Central Andes (31–33°S; Figure 1a) define type examples of Cordilleran orogenesis during Neogene flattening of the subducted oceanic plate, but debate persists regarding (1) the timing of shortening-induced exhumation along basement-involved ranges in the Frontal Cordillera hinterland
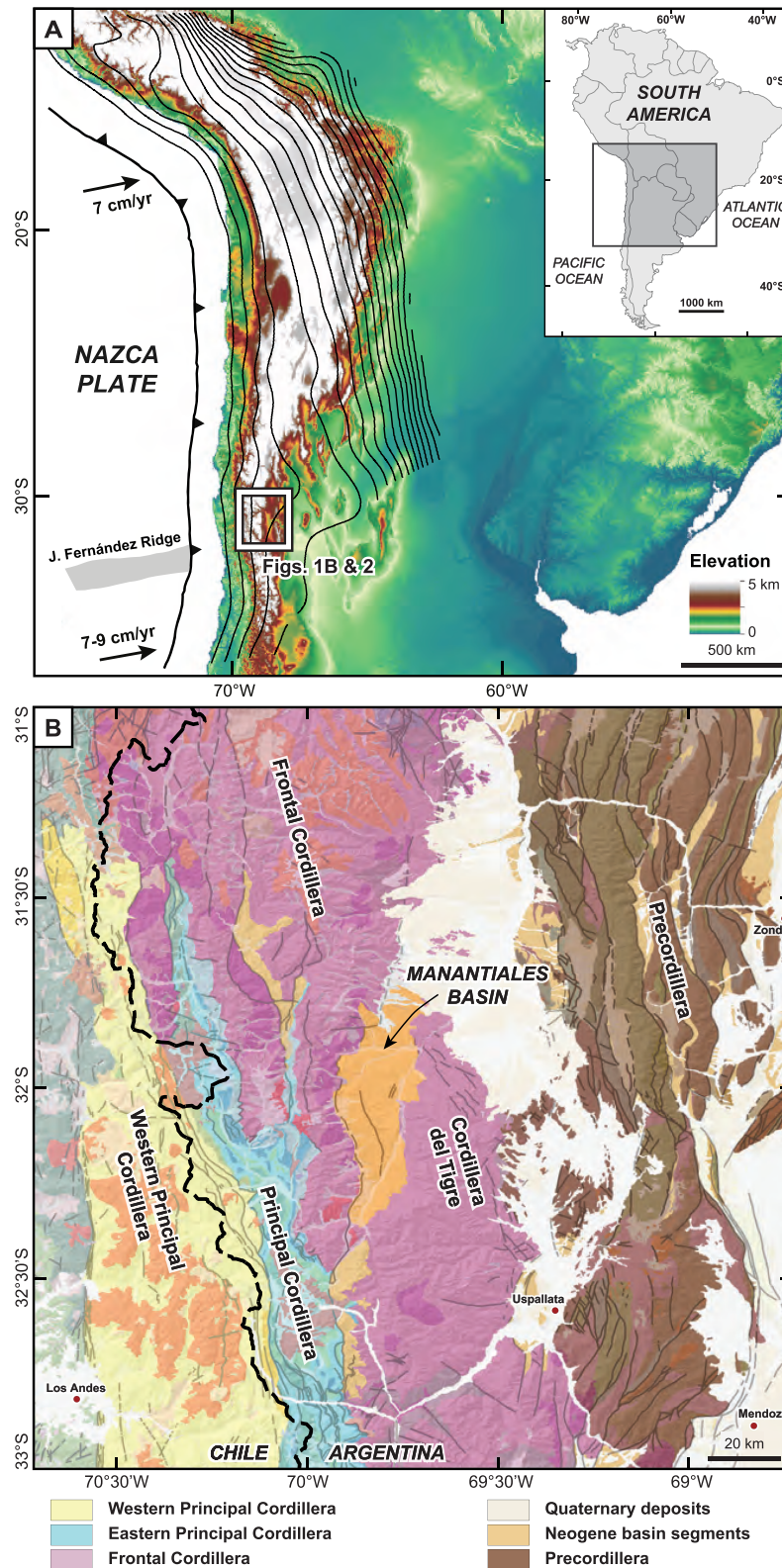
Fig 1. (a) Map of the Central Andes showing topography (ASTER DEM V002) and tectonic setting. Nazca-South America plate convergence rates after Ramos and Folguera (2009). Modern trench location and Wadati-Benioff zone contours (40 km contour interval; black lines) from the SLAB 2.0 model (Hayes et al., 2018). Inset illustrates location within South America. Box indicates location of Figures 1b and 2. (c) Map above the modern Chile-Argentina flat slab subduction segment highlighting major structural domains and Neogene foreland basins.

Fig 2. Geologic map of the study area showing cross-section trace (A-B-C) and sample locations for detrital zircon U-Pb geochronology and apatite (U-Th)/He thermochronology. Geology modified from Cristallini and Ramo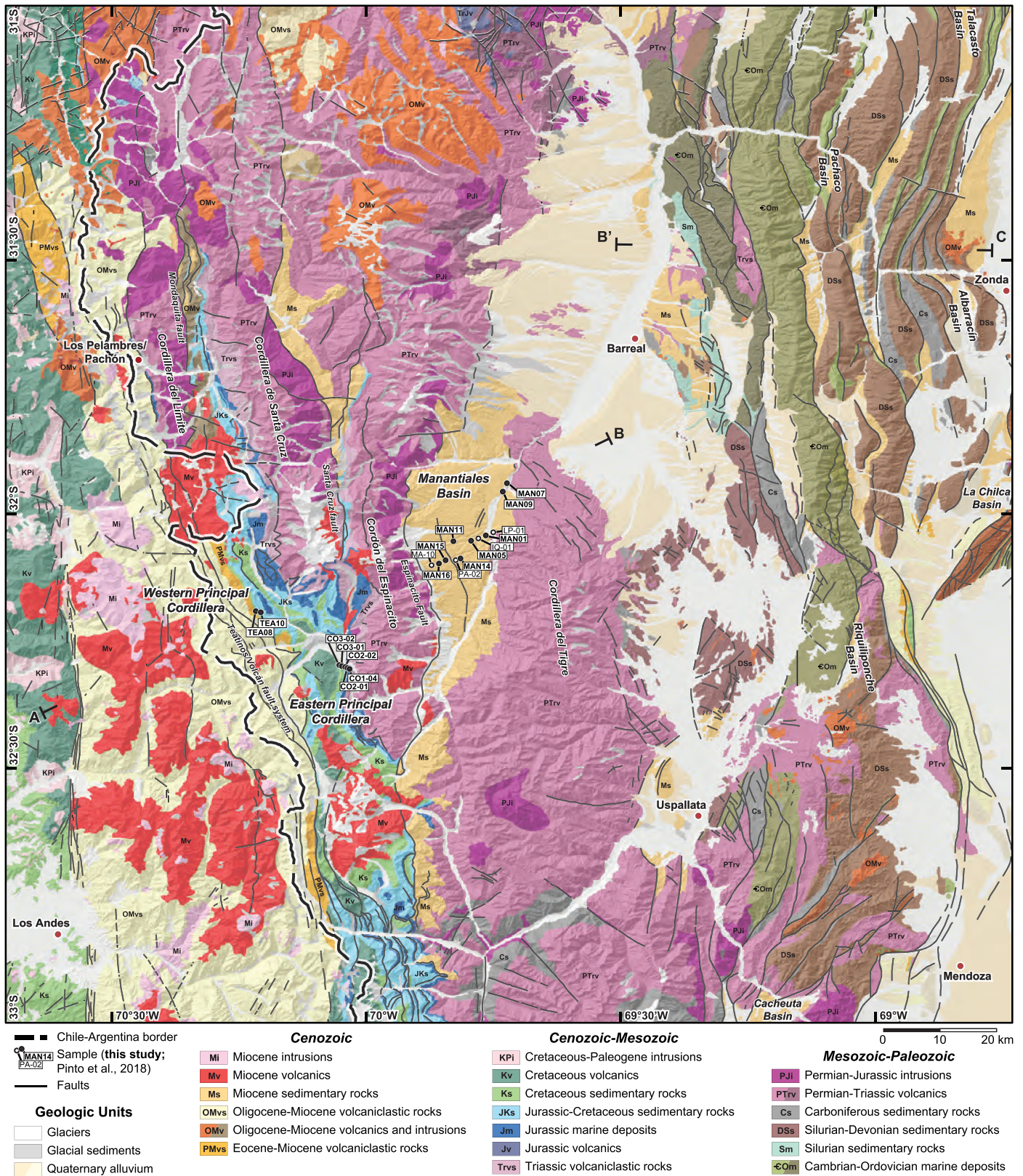s (2000), Jara and Charrier (2014), Mpodozis et al. (2009), Ragona et al. (1995), Rivano et al. (1993), Segemar (2000), and Sernageomin (2003).

domain (Figure 1b) and (2) the geometry of nonemergent structures, and potential structural linkages, between the retroarc hinterland and flanking fold-thrust belt. Previous studies have proposed a range of late Eocene–late Miocene ages for initial shortening and uplift of the Frontal Cordillera (~35 Ma, Lossada et al., 2017; ~25 Ma, Hoke et al., 2015; 24–17 Ma, Levina et al., 2014; 20–17 Ma, Buelow et al., 2018; Pinto et al., 2018; ~14–12 Ma, Jordan et al., 1996; Perez, 1995; ~9 Ma, Ramos & Folguera, 2009; 7 Ma, Rodríguez et al., 2018). Interpretations of regional structures that accommodate crustal thickening and transfer shortening from lower to upper crustal levels remain largely schematic and are complicated by limited exposures near the transition from basement-involved to thin-skinned deformation (Figures 1b, 2; Allmendinger et al., 1990; Allmendinger & Judge, 2014; Cristallini & Ramos, 2000; Ramos et al., 2004). However, recently published geochronological data for volcanic and sedimentary deposits along the Chile-Argentina border refine hinterland chronostratigraphy and sediment source characterization, providing new insights into provenance-based interpretations of exhumational timing (Jara & Charrier, 2014; Mackaman-Lofland et al., 2019; Maydagán et al., 2020; Mpodozis et al., 2009; Rodríguez et al., 2018). Broadband seismic data now available for Chile and western Argentina have additional potential to improve interpretations of nonemergent structures and better characterize the interactions between crustal thickening and shallow deformation (Alvarado et al., 2007; Ammirati et al., 2013, 2016; Gans et al., 2011).

In this study, we integrate new ^{40}Ar/^{39}Ar, detrital zircon U-Pb, and apatite (U-Th)/He results with published structural, geo/thermochronological, and geophysical data sets to (1) advance the chronostratigraphic and provenance framework of Neogene synorogenic deposits (preserved in the Manantiales Basin at ~32°S; Figures 1b and 2), (2) refine the timing of shortening-induced exhumation along major thin-skinned and basement-involved structures in the retroarc hinterland, and (3) investigate nonemergent structural geometries at ~32°S. Updated correlations with Neogene foreland basin deposits in the Precordillera fold-thrust belt allow us to reconstruct regional facies, sediment accumulation, and provenance trends (Buelow et al., 2018; Jordan et al., 1996; Levina et al., 2014; Pérez, 2001; Pinto et al., 2018). Thermokinematic modeling is applied to test middle to upper crustal structural interpretations (Almendral et al., 2015; Mora et al., 2015). Based on these results, we propose early to middle Miocene retroarc deformation involved south- and eastward migration of the foreland basin system during sequential exhumation along thin-skinned and basement-involved structures in the Principal and Frontal Cordilleras (Figures 1b, 2). Integrated structural, thermochronological, and geophysical data sets are further compatible with a hybrid thin- and thick-skinned décollement that connected retroarc hinterland and foreland domains. These findings quantify overriding plate deformation during changes in subduction zone geometry and provide insights into the relationships among thin- and thick-skinned shortening, exhumation, subsidence, and foreland basin evolution in Cordilleran mountain belts.

2. Geologic Context

The Andean orogen at 31–33°S is comprised of three structural domains: the Principal Cordillera, Frontal Cordillera, and Precordillera (Figures 1b, 2). The Principal Cordillera defines the western flank of the Andes and involves Mesozoic–Cenozoic sedimentary and volcanic deposits in principally thin-skinned deformation (Charrier et al., 2007; Cristallini & Ramos, 2000; Jara & Charrier, 2014; Ramos et al., 1996). The Frontal Cordillera is characterized by north trending uplifts that exhume chiefly mechanical basement in the form of upper Paleozoic–Triassic rhyolites and granitic intrusions, though Devonian–Carboniferous metamorphic and sedimentary rocks are exposed at the lowest structural levels (Heredia et al., 2002; Kleiman & Japas, 2009; Rocher & Vallecillo, 2014; Vallecillo et al., 2010). The Frontal Cordillera accommodated ~20 km of shortening and is made up of en échelon ranges exhumed along high-angle reverse faults (the Cordillera de Santa Cruz and Cordón del Espinacito, Figure 2; Cristallini & Ramos, 2000; Ramos et al., 2004). The Cordillera del Tigre comprises the easternmost range in the Frontal Cordillera at ~32°S; contractional faults are not mapped along the uplift margins (Figure 2; Heredia et al., 2012; Rocher & Vallecillo, 2014; Segemar, 2000). The Precordillera is a thin-skinned fold-thrust belt that accommodates the majority of retroarc shortening (>100 km) and involves Paleozoic–lower Mesozoic sedimentary deposits (Allmendinger et al., 1990; Cristallini & Ramos, 2000; Von Gosen, 1992).

Published cross sections and high-resolution local receiver function analyses provide insight into the structural interactions among these domains. High-amplitude positive arrivals beneath the central and western

Precordillera at ~5 and 10 km correspond with the depth and dip of the décollement calculated from balanced Precordillera cross sections (Ammirati et al., 2016; Cristallini & Ramos, 2000; von Gosen, 1992). Increased positive arrival depths beneath the western Precordillera and Cordillera del Tigre (from ~10 to 20 km) are also compatible with a change in detachment depth interpreted beneath the Precordillera and hinterland basement-cored ranges (e.g., Heredia et al., 2012).

Neogene synorogenic deposits are exposed in discontinuous, north trending basin segments throughout the Frontal Cordillera and Precordillera (Figure 2). Preserved stratigraphic thicknesses for these nonmarine deposits range from <1 km in the central Precordillera to >2–3 km for depocenters proximal to major Frontal Cordillera thrust faults (Buelow et al., 2018; Heredia et al., 2002; Irigoyen et al., 2000; Jordan et al., 1996; Levina et al., 2014; Pérez, 2001; Vergés et al., 2001).

The Manantiales Basin, located between the Cordón del Espinacito and Cordillera del Tigre at 31°45′–32°30′ S, contains ~3.6 km of nonmarine clastic deposits derived from the Principal and Frontal Cordilleras (Figures 1b, 2, 3; Alarcón & Pinto, 2015; Jordan et al., 1996; Perez, 1995; Pérez, 2001; Pinto et al., 2018; Ruskin et al., 2011). The western basin margin is overthrust by the Espinacito reverse fault, and to the east Manantiales strata overlie Permian–Triassic Choiyoi Group volcanic units in depositional contact (Figure 2; Cristallini & Ramos, 2000; Jordan et al., 1996). The exceptionally thick Neogene succession and western basin location provide a unique record of retroarc deformation and proximal foreland basin evolution near the transition from basement-involved to thin-skinned deformation styles.

3. Manantiales Basin Stratigraphy

Neogene Manantiales Basin deposits are assigned to the Chinches Formation and consist of (1) a basal member comprising ~40–350 m of cross-bedded eolian sandstones and scarce conglomerates; (2) a ~100 m thick andesitic breccia; and (3) an upper member of fluvial, alluvial fan, and lacustrine deposits that generally coarsen upsection and reach thicknesses >3,500 m (Figure 3; Jordan et al., 1996; Mirré, 1966; Perez, 1995). Detailed studies have identified four stratigraphic packages within the upper Manantiales Basin member (Jordan et al., 1996; Ruskin et al., 2011). The first package transitions from sandstone and mudstone facies representative of meandering river and floodplain environments to conglomeratic sandstones characteristic of braided fluvial deposition (Facies Groups I–III after Jordan et al., 1996; Figure 3). The second and third packages coarsen upward from lacustrine claystones and mudstones to braided fluvial sandstones and conglomerates (Groups IV–V, and VI–VII; Figure 3). The uppermost package begins with a thinner lacustrine interval than the underlying sequences and is capped by >600 m of boulder conglomerate; these deposits are located in the footwall directly east of the Espinacito reverse fault and are characteristic of an alluvial fan environment (Groups VI–VIII; Figures 2, 3; Cristallini & Ramos, 2000; Jordan et al., 1996; Pérez, 2001).

Paleocurrent measurements from this study (supporting information Table S1; eolian member) and Jordan et al. (1996; upper member) show generally east and southeast directed sediment transport throughout the Manantiales section (Figure 3), and previous studies have linked facies and provenance trends to thrust activity in the Principal and Frontal Cordilleras (Cristallini & Ramos, 2000; Jordan et al., 1996; Perez, 1995; Pinto et al., 2018). This study builds upon numerous investigations and data sets (e.g., clast counts, sandstone petrography, volcanic and sandstone geochemistry, heavy mineral analyses, zircon fission track and U-Pb geochronology, magnetostratigraphy, paleontology, and paleoaltimetry) that address the timing and nature of Manantiales Basin accumulation (Figure 3; Alarcón & Pinto, 2015; Hoke et al., 2014; Iglesia Llanos, 1995; Jordan et al., 1996; López et al., 2011; Perez, 1995; Pérez, 2001; Pinto et al., 2018; Ruskin et al., 2011).

4. Materials and Methods

4.1. ^{40}Ar/^{39}Ar Geochronology

Hornblende ^{40}Ar/^{39}Ar ages from the andesite breccia member (sample MAN09) and an ashfall tuff interbedded within the upper boulder conglomerate facies (MAN16) provide new constraints on the timing of Manantiales Basin accumulation (Figures 2, 3; Harrison, 1982). The andesite breccia sample (MAN09) contains plagioclase, K-feldspar, clinopyroxene, and abundant hornblende; the ashfall sample (MAN16)
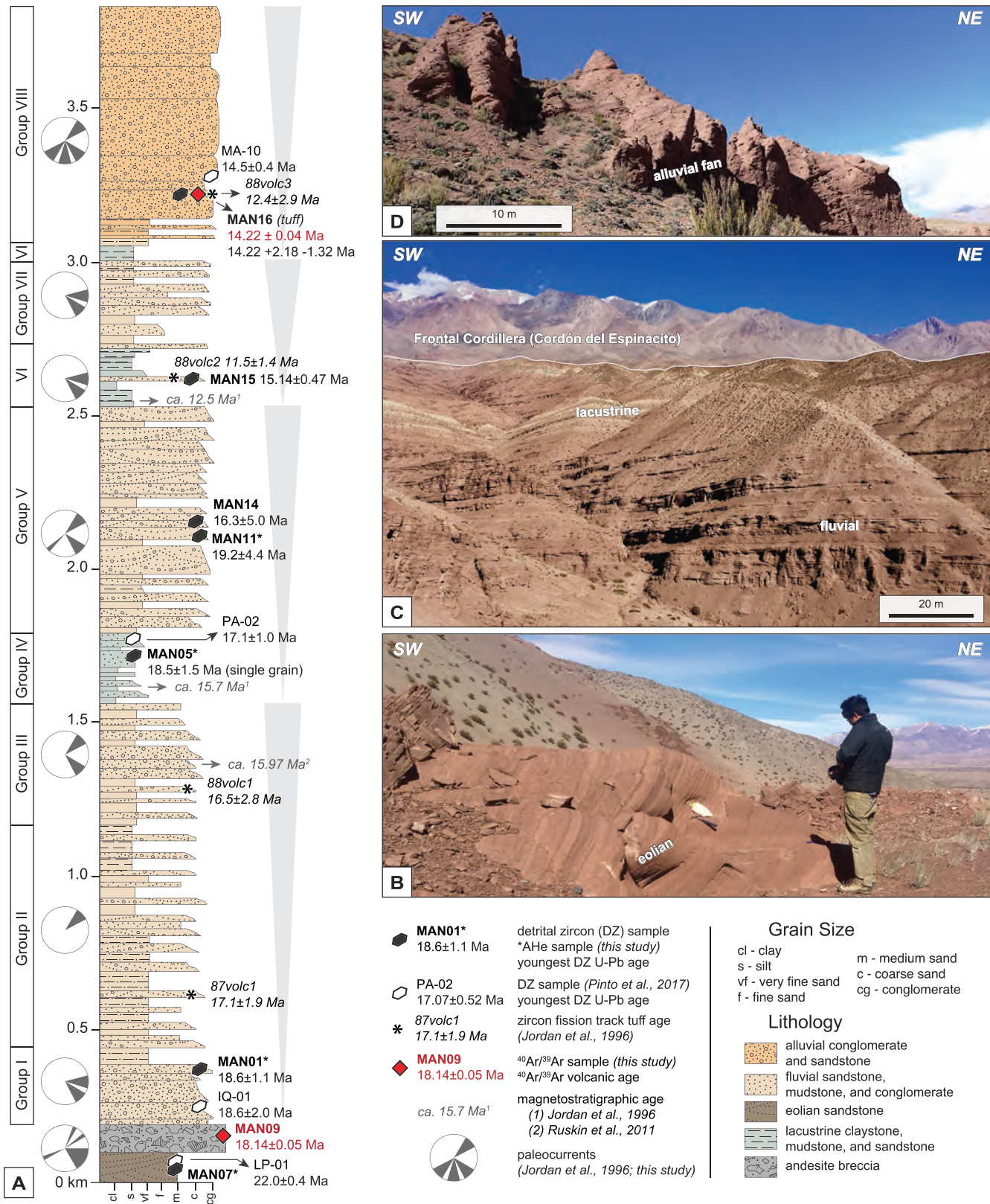
Fig 3. (a) Stratigraphic framework of the Manantiales Basin displaying sample locations and depositional age constraints. Groups I–VIII after Jordan et al. (1996). Gray triangles indicate upward-coarsening stratigraphic packages. (b) Field photo of basal eolian facies. (c) Landscape photo of fluvial and lacustrine deposits. Frontal Cordillera (Cordón del Espinacito) in background. (d) Photo showing alluvial fan facies near the Espinacito Fault (western basin margin).

comprises a ~20 cm horizon with K-feldspar and hornblende phenocrysts (Jordan et al., 1996; Pérez & Ramos, 1996). ^{40}Ar/^{39}Ar step heating analyses were performed for both samples at the New Mexico Geochronology Research Laboratory. Crystals were separated using conventional heavy liquid, magnetic, and handpicking techniques. Samples and flux monitors (Fish Canyon Tuff sanidine; Kuiper et al., 2008) were then loaded into machined AI discs and irradiated for 16 hours at the U.S. Geological Survey TRIGA reactor in Denver, Colorado. Step heating was conducted using a 55-W Photon Machines diode laser. ^{40}Ar/^{39}Ar isotopic measurements were made using a Helix MC Plus mass spectrometer. The New Mexico Geochronology Research Laboratory provides detailed operational information on their website (https://geoinfo.nmt.edu/labs/argon/methods/home.html). Additional instrumentation and step heating analytical parameters are reported in the supporting information (Table S2 and Data Set S2).

4.2. Zircon U-Pb Geochronology

Detrital zircon U-Pb geochronology yields provenance information and maximum depositional ages that provide additional constraints on the timing of basin accumulation. U-Pb age distributions were generated for six sandstone samples throughout the Manantiales Basin section ($n = 550$ concordant analyses; Figures 2, 3). Analyses were completed at the University of Texas at Austin following previously described procedures (Hart et al., 2016; Horton et al., 2016; Mackaman-Lofland et al., 2019; Thomson et al., 2017). Zircon grains were separated using standard magnetic and density separation techniques and mounted on double-sided tape attached to 1-inch-diameter acrylic disks. Zircon samples and standards (primary standard GJI zircon, Jackson et al., 2004) were analyzed using a Photon Machine Analyte G.2 Eximer laser (30-μm laser spot size) with a large-volume Helex sample cell and a Thermo Element2 inductively coupled plasma mass spectrometer. Data were reduced using VizualAge and Iolite software (Paton et al., 2010; Petrus & Kamber, 2012). At least 120 zircons were analyzed for each sample to obtain a statistically robust age and provenance data set (Vermeesch, 2004). Detailed analytical methods and raw data are reported in the supporting information (Table S3 and Data Set S3).

4.3. Apatite (U-Th)/He Thermochronology

Apatite (U-Th)/He (AHe) thermochronometry provides insight into the timing of tectonic and/or erosional exhumation in orogenic systems (e.g., Lock & Willett, 2008). AHe thermochronometry is based on the temperature-dependent retention of alpha particles (He) during radioactive decay of U, Th, and Sm and is characterized by a closure temperature range of ~50–110 °C that is widely applicable to upper-crustal processes (depending on grain size, radiation damage, and other factors; Ehlers & Farley, 2003; Farley & Stockli, 2002; Flowers et al., 2009; Reiners & Farley, 2001; Shuster et al., 2006). Exhumational cooling is commonly delayed following tectonic activity, and thermochronometric data do not directly quantify fault activity or surface uplift (e.g., Carretier et al., 2015; Kooi & Beaumont, 1996). However, if cooling is linked to fault-induced displacement and enhanced erosion, AHe ages may serve as a proxy for deformational timing (Ehlers & Farley, 2003; Lock & Willett, 2008; McQuarrie & Ehlers, 2017).

AHe analyses were conducted for 11 sandstone samples from (1) the Manantiales foreland basin, which was exhumed during uplift of the Cordillera del Tigre; (2) Mesozoic basin deposits in the Eastern Principal Cordillera, exhumed during uplift of the Cordón del Espinacito; and (3) deposits in the Western Principal Cordillera near the Chile-Argentina border (Figures 2, 3; Cristallini & Ramos, 2000; Jordan et al., 1996; Pérez, 2001; Ramos et al., 2004). Upper Paleozoic–Triassic igneous samples collected from key locations in the Cordillera del Tigre and Cordón del Espinacito hanging walls did not yield apatite suitable for analyses.

Measurements were completed at the University of Texas at Austin following analytical procedures described by Stockli et al. (2000) and Levina et al. (2014). Apatites were separated using the same magnetic and density techniques required for zircon minerals. Inclusion-free grains were then handpicked, photographed, and measured using a petrographic microscope (180x max) and sealed into platinum foil packets. When possible, six to eight euhedral, 70–150- μm-diameter crystals were selected per sample. However, several samples yielded very few, poor-quality apatites, and in these cases smaller (<60 μm) and/or slightly abraded grains were selected. To determine ^{4}He concentration, apatite samples and standards (Durango apatite; Boyce & Hodges, 2005) were laser degassed, cryogenically concentrated and purified, and analyzed using a noble gas quadrupole mass spectrometer. Sample aliquots were then dissolved using HNO_3-based solution spiked with a ^{235}U, ^{230}Th, and ^{149}Sm tracer; diluted with purified MilliQ water to 5% HNO_3; and
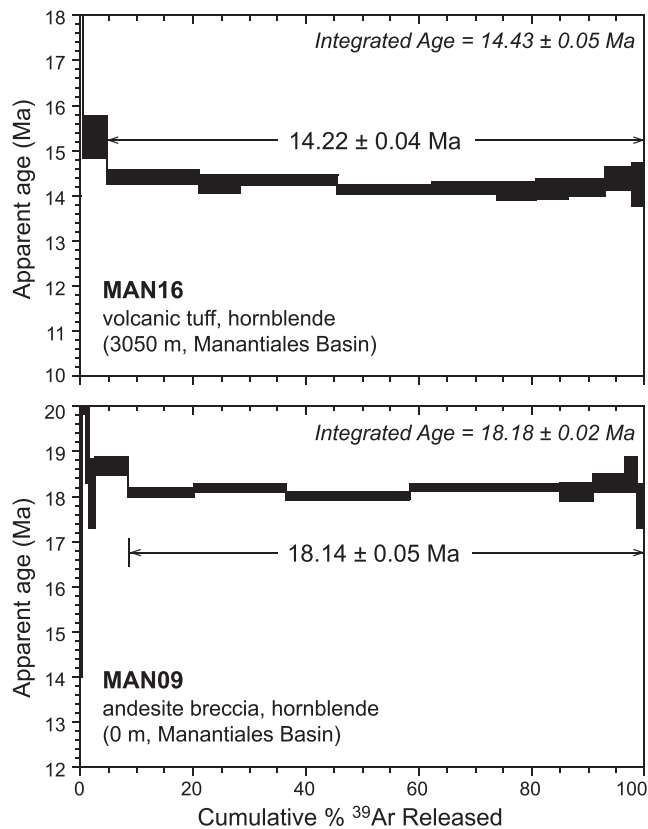
Fig 4. Hornblende ^{40}Ar/^{39}Ar age spectra for the andesite flow overlying the Manantiales Basin eolian facies (lower Manantiales Basin; MAN09) and volcanic tuff at the base of the alluvial fan facies (upper Manantiales Basin; MAN16). Plateau and integrated ages are reported as weighted mean ages with 1σ age uncertainties.

analyzed using a solution Thermo Element2 inductively coupled plasma mass spectrometer to measure ^{238}U, ^{235}U, ^{232}Th, and ^{147}Sm. Detailed analytical parameters and raw data are presented in the supporting information (Table S4 and Data Set S4).

5. Results

5.1. ^{40}Ar/^{39}Ar Results

^{40}Ar/^{39}Ar analyses for both Manantiales Basin samples yield overall flat age spectra, with minor discordance over the first 5% of gas released (Figure 4). K/Ca spectra show nearly constant values suggestive of pure, unaltered hornblende mineral separates. Isochron ages for the plateau segments are within uncertainty of the plateau ages for both samples (Data Set S2). The basal andesitic breccia (MAN09) yields a plateau age of 18.14 ± 0.05 Ma, and the upper interbedded tuff sample (MAN16) has a plateau age of 14.22 ± 0.04 Ma.

5.2. Zircon U-Pb Results

5.2.1. Potential Sediment Sources

We divide Manantiales detrital zircon U-Pb analyses (*n* = 550 total ages) into five signatures representative of potential sediment sources (Figure 5).

1. Proterozoic to mid-Paleozoic zircon ages (~350–1400 Ma, highlighted in gray) could have been recycled from Upper Cretaceous sedimentary rocks in the Principal Cordillera, upper Paleozoic metasedimentary and sedimentary rocks exposed along the Chilean coast, or Paleozoic strata in the Precordillera (Figures 1b, 2; Álvarez et al., 2011; Finney et al., 2005; Gleason et al., 2007; Hervé et al., 2013; Mackaman-Lofland et al., 2019; Naipauer et al., 2010; Ramos, 2009; Willner et al., 2008, 2012). Basement units toward the craton represent additional primary sources (Dahlquist et al., 2018; Rapela et al., 2007).

2. Late Paleozoic–Triassic ages (220–330 Ma, purple bars) were derived from rhyolitic and granitic units in the Frontal Cordillera and/or recycled from Mesozoic sedimentary rocks in the Principal Cordillera (Figures 1b, 2). Potential primary sources include the Elqui-Limari igneous complex in the westernmost Frontal Cordillera (~280–330 Ma), the regionally extensive Choiyoi Group igneous complex (~245–285 Ma), and post-Choiyoi plutonic and volcanic rocks exposed throughout the western and central Frontal Cordillera (220–245 Ma; Hervé et al., 2014; Kleiman & Japas, 2009; Maksaev et al., 2014; Mpodozis & Kay, 1992; Sato et al., 2015). Late Paleozoic–Triassic ages also comprise dominant components in the Mesozoic Principal Cordillera deposits; these spectra show an upsection trend toward older late Paleozoic–Triassic age peaks attributed to unroofing of the Frontal Cordillera (Mackaman-Lofland et al., 2019). All potential sources of late Paleozoic–Triassic U-Pb ages are characterized by high zircon fertility relative to other sources and age components, as reflected by the dominant late Paleozoic–Triassic components in Manantiales detrital spectra (Figure 5; Capaldi et al., 2017; Mackaman-Lofland et al., 2019).

3. Mesozoic ages (~80–220 Ma, blue bar) could have been recycled from latest Triassic–Cretaceous sedimentary and volcanic units in the Principal Cordillera or derived from intrusive and volcanic rocks exposed along the Chilean coast (Figures 1b, 2; Charrier et al., 2007, 2015; Jara & Charrier, 2014; Mackaman-Lofland et al., 2019; Pinto et al., 2018; Segemar, 2000; Sernageomin, 2003).

4. Latest Cretaceous–early Miocene zircons (~22–70 Ma, yellow bar) are present in andesitic-dacitic units and upper Paleogene–lower Miocene volcaniclastic rocks in the Western Principal Cordillera (Figures 1b, 2; Charrier et al., 2002, 2015; Jara & Charrier, 2014; Mackaman-Lofland et al., 2019; Mpodozis et al., 2009; Rivano & Sepúlveda, 1991). Paleogene retroarc basin deposits exposed along the eastern and southern margins of the Precordillera also contain ~22–70 Ma ages, but these units were likely not exposed until the late Miocene–Pliocene (Buelow et al., 2018; Fosdick et al., 2017).
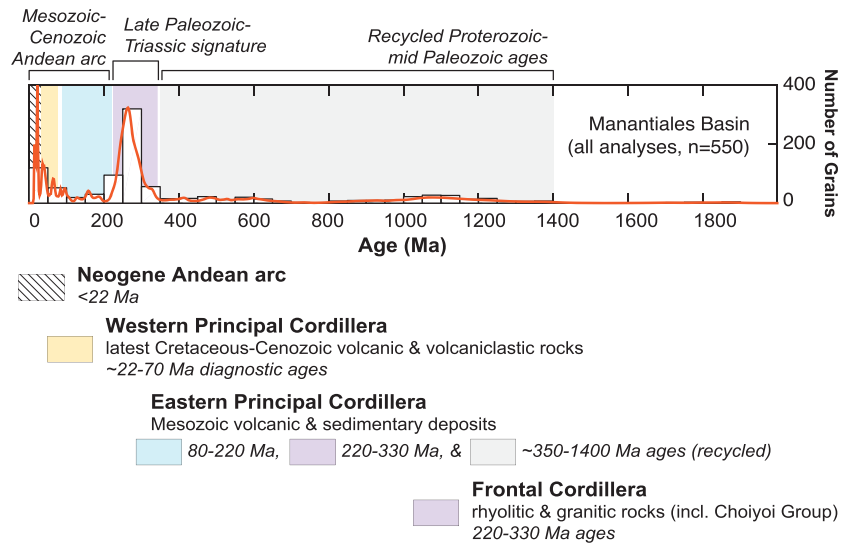
Fig 5. Age histograms and probability density plot (PDP) showing all detrital zircon U-Pb analyses for the Manantiales Basin (this study). Age signatures from potential sediment sources are highlighted in colored bars and discussed in the text.

5. Zircon ages <22 Ma (striped bar) were derived from the Neogene magmatic arc. Volcanic centers were concentrated in the Western Principal Cordillera until ~17 Ma, and spread eastward to the Principal Cordillera, Frontal Cordillera, and Precordillera during Manantiales accumulation (Figures 1b, 2; Cristallini & Ramos, 2000; Jara & Charrier, 2014; Kay & Mpodozis, 2002; Segemar, 2000).

5.2.2. Stratigraphic Trends

Our detrital zircon U-Pb results (six sandstone samples, $n = 550$ concordant analyses) augment detrital zircon data recently published by Pinto et al. (2018) for the same stratigraphic section (four sandstone samples, $n = 422$ analyses). We integrate both data sets to characterize chronostratigraphic and provenance trends in the Manantiales Basin (Figure 6).

U-Pb age distributions for the basal eolian facies are dominated by latest Cretaceous–early Miocene (~22–70 Ma) zircon ages (Figures 6a, 6b). Late Paleozoic–Triassic ages (~220–330 Ma) make up subordinate components, and Mesozoic (~80–220 Ma) and Proterozoic to mid-Paleozoic (~350–1400 Ma) grains are relatively limited in both samples (MAN07 and LP-01). Sample MAN07 did not contain zircons <40 Ma, but LP-01 yields a 22.0 ± 0.4 Ma maximum depositional age that constrains the timing of initial basin accumulation (Figure 6b; Pinto et al., 2018).

Fluvial and lacustrine deposits overlying the Manantiales andesitic breccia record a shift in U-Pb age spectra. Results from the lower two stratigraphic packages display dominant late Paleozoic–Triassic (220–330 Ma) components and reduction of the latest Cretaceous–early Miocene signature (Figures 3, 6c–6h). The concurrent increase in Mesozoic and Proterozoic to mid-Paleozoic components is also significant given the low proportion of ~80–220 and ~350–1400 Ma zircon ages throughout the Manantiales detrital spectra (Figures 5, 6c–6h). Late Paleozoic–Triassic age peaks from the second stratigraphic package signify a slight upsection shift toward younger ages, from ~280 Ma in MAN05 to ~265 Ma, with a secondary ~240 Ma peak, in MAN14 (Figures 6e–6h).

Lacustrine and proximal alluvial fan deposits in the third and fourth stratigraphic packages show increased latest Cretaceous–early Miocene (~22–70 Ma) signatures, disperse late Paleozoic–Triassic (220–330 Ma) ages, and decreased Mesozoic (~80–220 Ma) and Paleozoic to mid-Proterozoic (350–1400 Ma) components relative to underlying detrital spectra (MAN15 and MA-10; Figures 3, 6i–j).

All results from the fluvial, lacustrine, and alluvial fan deposits in the upper Manantiales Basin contain <22 Ma zircons derived from the Neogene Andean arc. With the exception of sample MAN11, maximum depositional ages systematically decrease from 18.6 ± 2.0 and 18.6 ± 1.1 Ma in the lower meandering river and floodplain deposits (IQ-01 and MAN01) to 14.5 ± 0.4 Ma in the upper boulder conglomerates (MA-10; Figures 3, 6c–6j; Pinto et al., 2018).
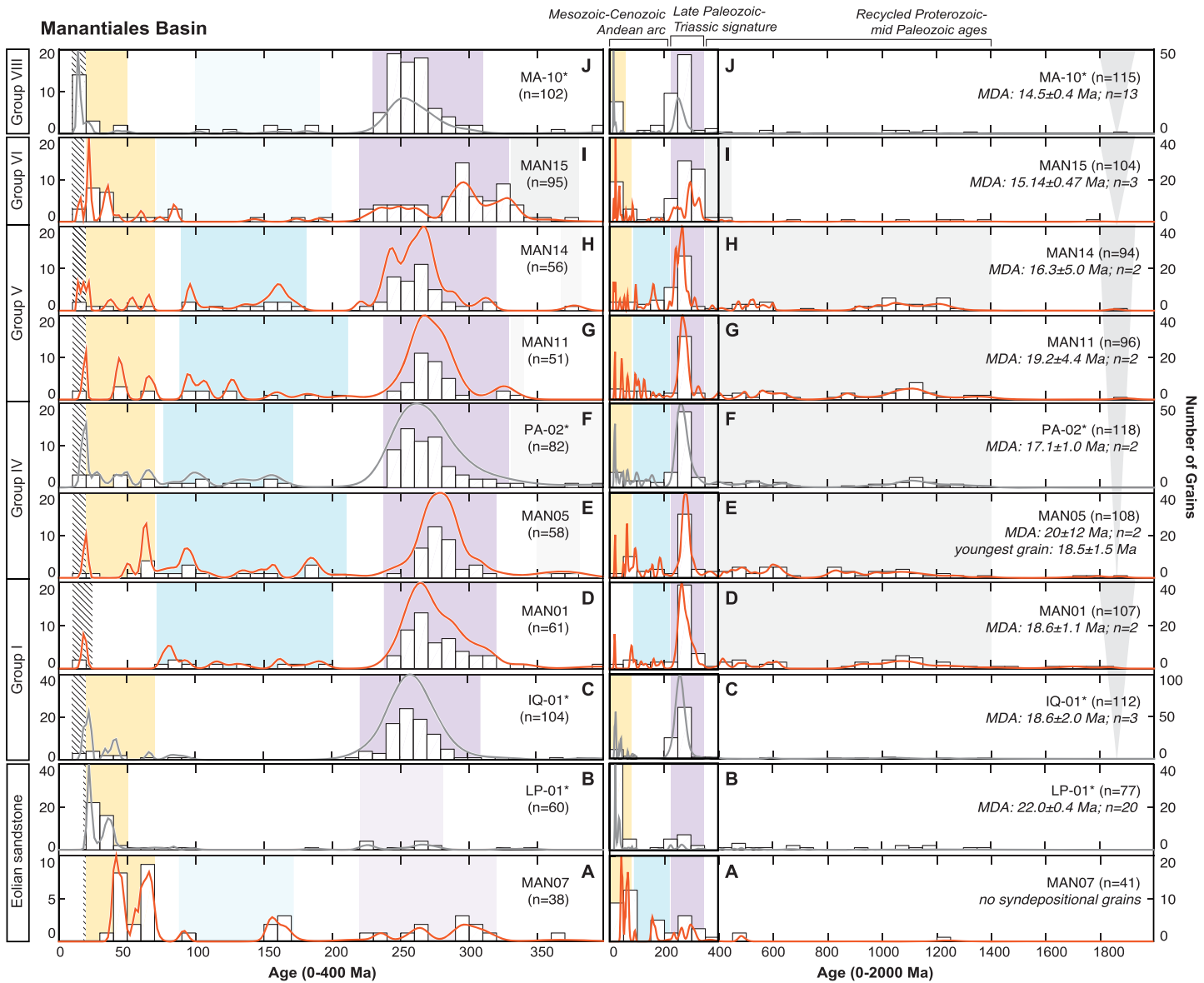
Fig 6. Age histograms and probability density plots (PDPs) showing detrital zircon U-Pb results for the Manantiales Basin. Analyses from this study are shown in orange PDPs; results from Pinto et al. (2018) in gray. Results are arranged in stratigraphic order (6a–6j). Gray triangles indicate upward-coarsening stratigraphic packages. Right column displays the full distribution of zircon U-Pb ages (0–2000 Ma). Left column shows 0–400 Ma interval for the same samples. Colored bars represent provenance signatures from the Principal and Frontal Cordilleras (Figure 5). Striped bars denote syndepositional volcanic components.

5.3. Apatite (U-Th)/He Results

AHe results are younger than the geochronological age constraints for the same samples, indicating that the three analyzed transects were thermally reset by postdepositional burial reheating (Mackaman-Lofland et al., 2019; Pinto et al., 2018). Results do not show significant correlation between AHe age and grain size or effective uranium concentration, and of the 61 total apatite grains analyzed, 10 were rejected due to blank-level ^{4}He concentrations, high ^{4}He reextract measurements (indicative of He-rich inclusions within the crystal), and/or statistically irreproducible aliquot ages (outside 2σ confidence interval for mean sample age; Vernon et al., 2009; Table S4).

AHe age-depth relationships are shown with respect to stratigraphic level within the Neogene (Figure 7a) and Mesozoic (Figures 7b, 7c) basin sections (Cristallini & Ramos, 2000; Jordan et al., 1996). Uncertainty-weighted linear regression of positive cooling age-stratigraphic level relationships in the
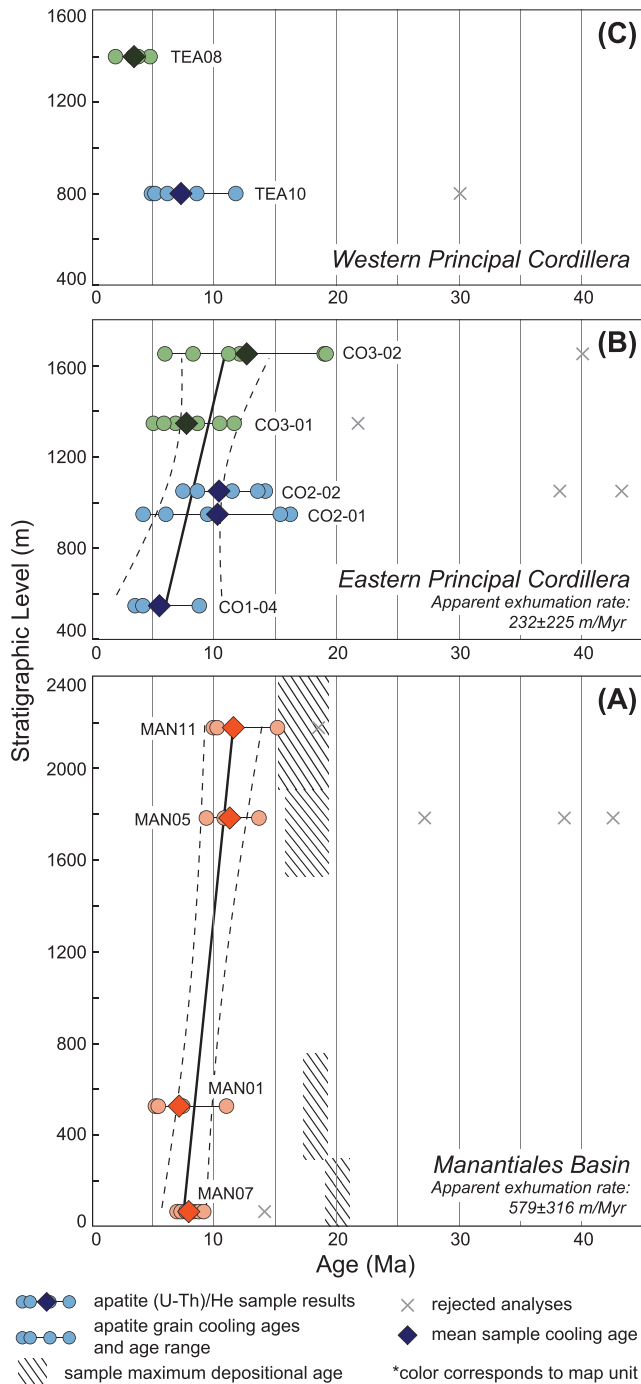
Fig 7. Plots displaying apatite (U-Th)/He cooling ages versus stratigraphic level for (a; orange points) the Manantiales Basin deposits and (b, c; green and blue points) Mesozoic sedimentary rocks in the Principal Cordillera. The (a) Manantiales Basin and (b) Eastern Principal Cordillera plots show positive weighted regression relationships (solid black lines) and 2σ confidence interval (dashed black lines).

Manantiales Basin and Eastern Principal Cordillera yields apparent exhumation rates (Figures 7a, 7b). However, these values erroneously assume that all samples followed vertical exhumation paths and do not account for changes in the thermal field due to topography or faulting. Given the aforementioned assumptions and large sample uncertainties, we emphasize that apparent exhumation rates should not be considered representative of geological exhumation (e.g., Huntington et al., 2007).

AHe cooling ages from the Manantiales Basin range between 5.2 ± 0.3 and 15.1 ± 0.9 Ma and show reasonable within-sample reproducibility (~4–7 Myr aliquot ranges; Figure 7a). The majority of ages cluster at ~6.5–12 Ma and are consistently younger than zircon maximum depositional ages for the same samples. Cooling ages show a positive correlation with stratigraphic level, increasing from mean ages of 8.9 ± 2.5 and 7.2 ± 2.6 Ma in the lower Manantiales Basin deposits (MAN07 and MAN01) to 11.7 ± 2.9 Ma at 2,200 m (MAN11). Uncertainty-weighted regression of this relationship indicates an apparent exhumation rate of 579 ± 316 m/Myr (Figure 7a).

The Eastern Principal Cordillera samples yield AHe ages between 3.6 ± 0.2 and 19.1 ± 1.1 Ma and show a similar upsection trend toward older ages (Figure 7b). Aliquot ages for CO1-04, CO2-02, and CO3-01 are reproducible within the same ~4–7 Myr range specified for Manantiales Basin results, but CO2-01 and CO3-02 show greater within-sample data dispersion (>10 Myr aliquot age ranges). Most Eastern Principal Cordillera ages fall between 5 and 14 Ma, and mean cooling ages systematically increase from 5.4 ± 2.8 Ma at 550 m (CO1-04) to 12.7 ± 5.5 Ma at 1,650 m (CO3-02). The slightly younger 7.9 ± 2.6 Ma mean age at 1,350 m (CO3-01) remains within error of the overall positive age-stratigraphic level correlation. Uncertainty-weighted regression reflects the greater dispersion in the Eastern Principal Cordillera data set and yields an apparent exhumation rate of 232 ± 225 m/Myr (Figure 7b).

AHe results from the Western Principal Cordillera show the youngest cooling ages, with the majority clustered between 2.5 and 8 Ma (Figure 7c). Sample TEA10 contains a <7 Myr spread in aliquot ages and has a mean age of 7.1 ± 2.8 Ma, and TEA08 yields a highly reproducible age of 3.3 ± 1.2 Ma. The limited data set and negative age-stratigraphic level relationship precludes a linear regression.

6. Interpretations

6.1. $^{40}Ar/^{39}Ar$ Interpretation

As the initial steps display greater discordance (over the first 5% of gas released), plateau ages are considered representative of depositional ages for both samples. The plateau age obtained for the basal andesitic breccia (18.14 ± 0.05 Ma; MAN09) is compatible with detrital zircon maximum depositional ages calculated for underlying eolian and overlying fluvial facies (21.16 ± 0.49 and 18.7 ± 2.0 Ma, respectively; Figures 3, 4; Pinto et al., 2018). Previous age estimates were based on geochemical correlations with dated andesitic volcanic deposits in the Cordón de La Ramada and near Barreal (~20 Ma; Alarcón & Pinto, 2015; Leveratto, 1976; Perez, 1995; Pérez, 2001), and these $^{40}Ar/^{39}Ar$ data represent the first isotopic ages obtained for the andesite breccia member. The 14.22 ± 0.04 Ma plateau age for the upper interbedded tuff (MAN16) is also consistent with maximum depositional ages from under- and overlying strata (15.14 ± 0.47 to $13.83 \pm$

0.45 Ma; this study; Pinto et al., 2018) and within error of the 12.4 ± 2.9 Ma zircon fission track age obtained for the same horizon (Figures 3, 4; Jordan et al., 1996).

6.2. Zircon U-Pb Interpretation
6.2.1. Potential Sediment Sources

Regional provenance and structural indicators suggest that exhumation and topographic uplift of the Andes initiated by the early to middle Miocene, severely limiting sediment transport from coastal sources during Manantiales Basin accumulation (Cristallini & Ramos, 2000; Hoke et al., 2014; Jordan et al., 1996; Maydagán et al., 2020; Perez, 1995; Pérez, 2001; Pinto et al., 2018; Rodríguez et al., 2018). Paleocurrent indicators are further incompatible with sediment derivation from eastern domains (Figure 3; Jordan et al., 1996). As such, we consider latest Cretaceous–early Miocene zircon ages (~22–70 Ma) diagnostic of sediment contribution from the Western Principal Cordillera (Figures 5, 6). Following Western Principal Cordillera uplift, the combined presence of Mesozoic (~80–220 Ma), late Paleozoic–Triassic (220–330 Ma), and Proterozoic to mid-Paleozoic (~350–1400 Ma) ages is most consistent with recycling from Triassic–Cretaceous sedimentary rocks in the central and Eastern Principal Cordillera. Late Paleozoic–Triassic (220–330 Ma) components also define igneous sources in the Frontal Cordillera, but component associations and unroofing trends in the late Paleozoic–Triassic age peaks help distinguish igneous from recycled sedimentary sources.

In this context, eastward (cratonward) advance of the thrust belt and sequential unroofing of the Principal and Frontal Cordilleras should result in (1) the introduction of ~22–70 Ma Western Principal Cordillera ages in basal foreland basin deposits; (2) decreased Western Principal Cordillera signatures and the combined introduction of ~80–220, 220–330, and ~350–1400 Ma ages during thrust propagation to the Eastern Principal Cordillera; and (3) shutoff of Principal Cordillera provenance signatures, recycling of older foreland basin strata, and persistent late Paleozoic–Triassic components during exhumation of the Cordón del Espinacito along the western Manantiales Basin margin (Figure 2).

6.2.2. Stratigraphic Trends

The latest Cretaceous–early Miocene (~22–70 Ma) zircon age components that dominate basal eolian detrital spectra strongly indicate sediment derivation from the Western Principal Cordillera (Figures 6a, 6b). Hinterland structural relationships further suggest shortening-induced exhumation along faults at the eastern domain margin by 22–18 Ma (e.g., Teatinos/Volcán fault system, Figure 2; Cristallini & Ramos, 2000; Jara & Charrier, 2014; Pérez & Ramos, 1996; Ramos & Folguera, 2005). Subordinate late Paleozoic–Triassic (~220–330 Ma) age components may reflect erosion from Choiyoi Group deposits at the Manantiales Basin margins, recycling from Mesozoic units in the Principal Cordillera, and/or exhumation of distal igneous sources in the Cordillera del Límite (located along strike of the Teatinos/Volcán fault system, Figure 2; Mirré, 1966; Cristallini & Ramos, 2000; Pinto et al., 2018).

The combined increase in Mesozoic (~80–220 Ma) and Proterozoic to mid-Paleozoic (~350–1400 Ma) components following the shift to fluvial and lacustrine deposition is consistent with sediment recycling from Mesozoic sources in the central and Eastern Principal Cordillera (Figures 5, 6c–6h). Dominant late Paleozoic–Triassic (~220–330 Ma) components could have been derived from the Principal or Frontal Cordilleras, but the upsection shift toward younger late Paleozoic–Triassic age peaks (Figures 6e–6h), coupled with diagnostic Principal Cordillera age signatures in the same samples, points to reverse unroofing and component recycling during Principal Cordillera exhumation (e.g., Mackaman-Lofland et al., 2019; Pérez, 2001). Choiyoi Group units in the Cordillera de Santa Cruz represent a probable additional source of late Paleozoic–Triassic ages (Figure 2; Jordan et al., 1996; Pérez & Ramos, 1996).

We interpret the reduction in Mesozoic (~80–220 Ma) and Paleozoic to mid-Proterozoic (350–1400 Ma) components in the third and fourth stratigraphic packages to reflect diminished contribution from the Eastern Principal Cordillera (Figures 6i, 6j). Latest Cretaceous–early Miocene (~22–70 Ma) ages may indicate renewed contribution from the Western Principal Cordillera and bypass across the central and Eastern Principal Cordillera domains, or recycling of subjacent foreland basin deposits. The broad range of late Paleozoic–Triassic ages and coeval shift to coarse depositional facies are compatible with the introduction of varied or recycled sources, potentially including recycled foreland basin strata and/or primary late Paleozoic–Triassic sources in the Cordón del Espinacito, proximal to the Manantiales depocenter (Mackaman-Lofland et al., 2019; Pinto et al., 2018).

6.3. Apatite (U-Th)/He Interpretation

No evidence of middle Miocene–Pliocene normal faulting is documented in the Andean retroarc at 31–33°S, and the foreland basin record suggests ongoing shortening, thrust loading, and flexural subsidence during cooling of the Manantiales and Principal Cordillera AHe transects (Figure 7; Buelow et al., 2018; Jordan et al., 2001). As such, we interpret AHe results to reflect exhumational cooling in response to shortening-induced uplift and enhanced erosion. Positive cooling age-stratigraphic level relationships in the Manantiales Basin and Eastern Principal Cordillera further suggest discrete exhumation along the Cordillera del Tigre and Espinacito fault, rather than a regional erosional event (Figures 2, 7a, 7b). We interpret the negative age-stratigraphic level relationship in the Western Principal Cordillera to reflect deformation and tilting of the Mesozoic sedimentary rocks prior to exhumation above the AHe closure isotherm, consistent with crosscutting relationships that confirm thin-skinned shortening in the Principal Cordillera before 9–12 Ma (Cristallini & Ramos, 2000; Jara & Charrier, 2014).

Overlying basin deposits may have been of sufficient thickness to reset AHe ages in the lower Manantiales section, but a combination of depositional and thrust sheet burial was likely required to reset the sedimentary rocks in the Principal Cordillera (Cristallini & Ramos, 2000). Results from all three transects indicate substantial exhumation throughout the Andean hinterland and retroarc regions over the past ~14 Myr, with the majority of Cordillera del Tigre and lower Manantiales Basin cooling from ~12 to 6.5 Ma, unroofing of the upper Espinacito Fault hanging wall from ~14 to 5 Ma, and late-stage exhumation near the Chile-Argentina border at ~8–2.5 Ma.

7. Discussion

7.1. Manantiales Basin Accumulation History

$^{40}Ar/^{39}Ar$ results and this study's zircon maximum depositional ages are combined with published detrital zircon, zircon fission track, and paleomagnetic data sets to refine the chronostratigraphy of the Manantiales Basin and evaluate sediment accumulation trends (Figure 8a). The maximum depositional age obtained for the basal eolian member indicates initial subsidence at 22.0 $\pm$ 0.4 Ma (Pinto et al., 2018). $^{40}Ar/^{39}Ar$ volcanic ages constrain deposition of the fluvial and lacustrine facies (Groups I–VII; Figure 3) to 18.14 $\pm$ 0.05 to 14.22 $\pm$ 0.04 Ma. With the exception of the zircon fission track age near 2.5-km stratigraphic level, all $^{40}Ar/^{39}Ar$, zircon fission track, and maximum depositional age constraints are within error throughout the Manantiales section (Jordan et al., 1996; Pinto et al., 2018). Isotopic ages are consistently several million years older than preferred paleomagnetic age interpretations (Figure 3; Jordan et al., 1996; Ruskin et al., 2011) but align with Jordan et al. (1996)'s alternative magnetic polarity correlation in which fluvial and lacustrine deposition spanned ~19 to 13.3 Ma.

Age-thickness data reveal slow (<90 m/Myr) sediment accumulation during initial subsidence and eolian deposition, followed by rapid (average >750 m/Myr) accumulation during fluvial and lacustrine deposition (Groups I–VII; Figure 8a). Inflections in the accumulation curve at ~18, ~17, and ~15 Ma additionally correspond with the first through third upward-coarsening stratigraphic packages (Figures 3, 8a; Jordan et al., 1996). Age data and accumulation rates have yet to be obtained for the uppermost boulder conglomerate deposits (upper Group VIII), but the sigmoidal shape of the Manantiales accumulation history is diagnostic of flexural subsidence and distal foreland to wedge-top depocenter migration (DeCelles & Horton, 2003; Horton & Decelles, 2001).

7.2. Manantiales Basin Provenance (Multidimensional Scaling)

We use a multidimensional scaling analysis (MDS) based on the Kolmogorov-Smirnov test D value to statistically discriminate detrital zircon age distributions and evaluate trends in Manantiales Basin provenance (Figure 8b). MDS maps pairwise sample dissimilarity as spatial proximity, such that statistically similar samples plot closely together and dissimilar samples plot further apart (Vermeesch, 2013). We compare detrital zircon age distributions for individual Manantiales Basin samples (this study; Pinto et al., 2018) with composite zircon age distributions representative of Western Principal Cordillera, Eastern Principal Cordillera, and Frontal Cordillera sources. Eight detrital samples ($n = 585$ total ages) from Mackaman-Lofland et al. (2019)'s Western La Ramada Basin transect were integrated to represent the Western Principal Cordillera source; nine detrital samples ($n = 520$ ages) from the Central La Ramada
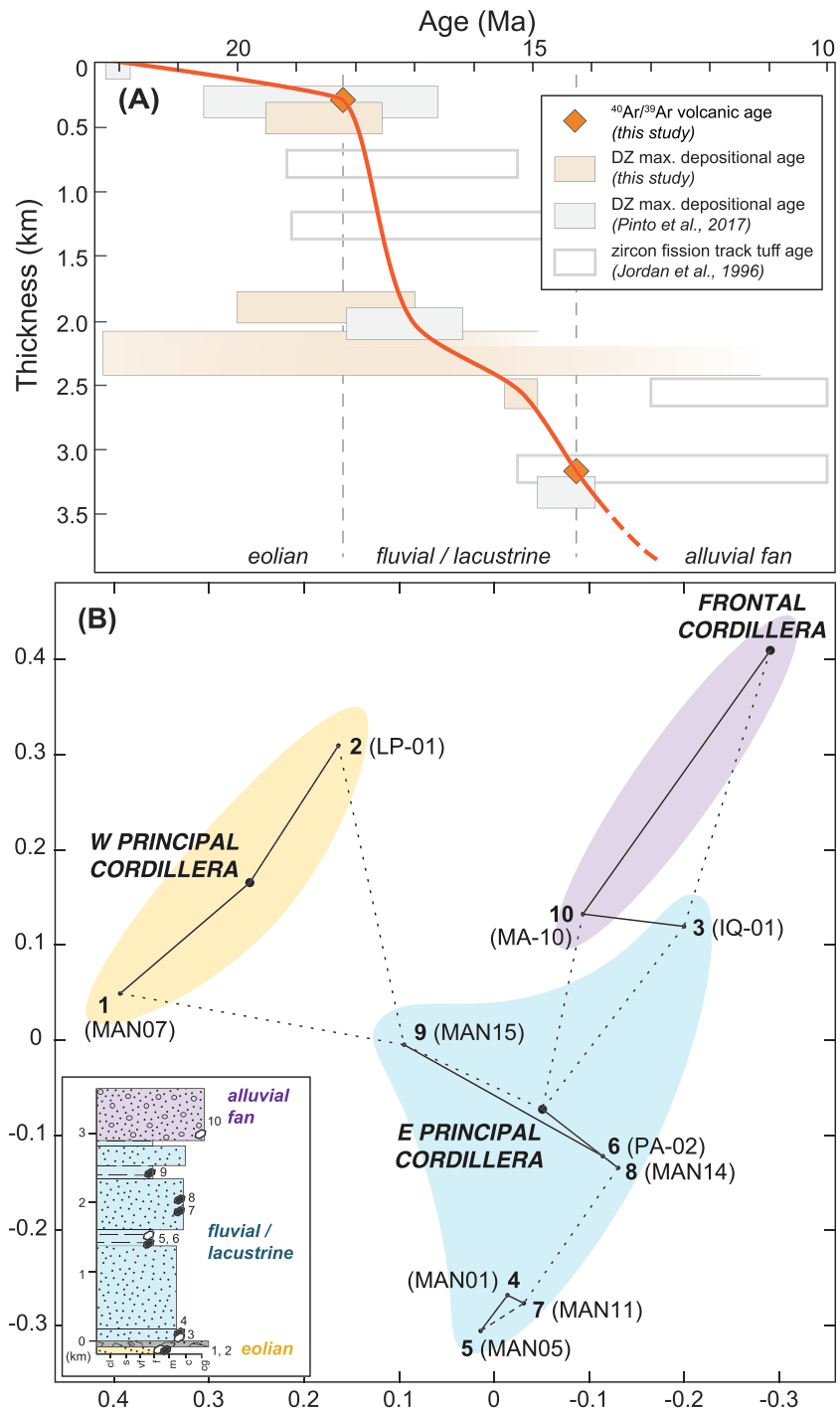
Fig 8. (a) Stratigraphic age versus thickness diagram for the Manantiales Basin. (b) Multidimensional scaling (MDS) plot showing relative statistical similarity (Komolgorov-Smirnov test *D* value; Vermeesch, 2013) between Manantiales Basin detrital zircon samples and composite zircon age distributions representative of potential sediment sources (Western Principal Cordillera, Eastern Principal Cordillera, and Frontal Cordillera; Mackaman-Lofland et al., 2019; Pinto et al., 2018). Inset shows sample locations within the Manantiales section. Symbols are explained in Figure 3.

Basin transect comprise the Eastern Principal Cordillera data set; and one igneous sample (ESP02, *n* = 29 ages) represents the Cordón del Espinacito (Mackaman-Lofland et al., 2019).

U-Pb age distributions from the basal eolian facies (MAN07 and LP-01; shown in yellow, Figure 8b) plot closest to the composite age distribution from the Western Principal Cordillera. Samples from the fluvial and

lacustrine deposits that overlie the Manantiales andesite breccia (highlighted in blue) plot in a field surrounding data compiled from Mesozoic sedimentary rocks in the Eastern Principal Cordillera. The sample from the upper boulder conglomerate (MA-10; purple) maps closest to the age distribution from the Cordón del Espinacito at the western basin margin (Mackaman-Lofland et al., 2019). Finally, U-Pb age distributions from the upper Manantiales stratigraphic packages show close provenance associations with samples from the base of the Manantiales succession: MA-10 (from the upper boulder conglomerate) maps nearest to IQ-01 (collected directly above the andesite breccia), and MAN15 (from the upper lacustrine deposits) shows affinity with MAN07 and LP-01 (from the basal eolian facies). Collectively, MDS associations indicate (1) sediment derivation from the Western Principal Cordillera during initial eolian deposition; (2) provenance from Mesozoic sources in the Eastern Principal Cordillera following the shift to fluvial and lacustrine environments; and (3) foreland basin recycling and detrital contribution from the Cordón del Espinacito during uppermost fluvial-lacustrine and alluvial fan accumulation.

7.3. Foreland Basin Evolution

We integrate sedimentological, geo/thermochronological, provenance, and structural constraints to reconstruct Manantiales Basin evolution and determine the timing of deformation in the Principal and Frontal Cordilleras (Figure 9). Comparable data sets have been obtained for Neogene synorogenic deposits in the Precordillera (La Chilca, Riquiliponche, Pachaco, Talacasto, and Albarracín depocenters; Levina et al., 2014; Pinto et al., 2018; Reyna et al., 2010) and the Cacheuta foreland basin, located south of the Precordillera at 33°S (Figures 2, 10; Buelow et al., 2018). We update correlations between these basin segments to investigate retroarc accumulation trends and provide insight into proximal-distal foreland basin evolution.

7.3.1. Distal Foreland Basin Accumulation (Late Oligocene–Early Miocene)

Manantiales Basin accumulation began at ~22 Ma with the development of an eolian system, deposited unconformably on Permian–Triassic Choiyoi Group igneous units (Mirré, 1966; Pérez, 2001; Pinto et al., 2018). Zircon U-Pb results, published geochemical, detrital heavy mineral, and sandstone petrographic data sets, and hinterland structural relationships all point to sediment contribution from the Western Principal Cordillera during shortening-induced exhumation along structures at the eastern domain margin (Teatinos/Volcán and related fault systems, Figure 2; Alarcón & Pinto, 2015; Cristallini & Ramos, 2000; Jara & Charrier, 2014; Mackaman-Lofland et al., 2019; Pérez, 2001; Pinto et al., 2018; Piquer et al., 2017). Subordinate late Paleozoic–Triassic igneous components may reflect both Principal Cordillera basin recycling and exhumation of primary sources in the Cordillera del Límite (Figure 9a; Cristallini & Ramos, 2000; Mirré, 1966). The eolian facies and slow sedimentation rates (<90 m/Myr) are compatible with distal foreland basin accumulation during initial thrust loading and flexural subsidence (Figures 8a, 9a).

To the south and east, deposition initiated with ephemeral fluvial and playa lake conditions in the Precordillera basins (at ~24 Ma) and episodic, sheet-flow-dominated fluvial/alluvial fan accumulation in the Cacheuta basin (~20 Ma) and transitioned to a regionally extensive eolian system by ~18 Ma (Figures 10a, 10b; Buelow et al., 2018; Jordan et al., 1993, 2001; Levina et al., 2014). Provenance results reveal ubiquitous Western Principal Cordillera and late Paleozoic–Triassic components comparable to the lower Manantiales Basin deposits, with substantial Neogene ages derived from the Andean magmatic arc (Buelow et al., 2018; Levina et al., 2014). Greater syndepositional volcanic contributions to the Precordillera and Cacheuta basin segments may reflect distal ash accumulation during prevailing south and southeast directed wind conditions (Figure 3). Rare Mesozoic ages in the basal Cacheuta detrital zircon spectra likely attest to the involvement of Mesozoic strata along faults at the eastern margin of the Western Principal Cordillera at 33°S (Figure 2; Buelow et al., 2018; Cristallini & Cangini, 1993).

7.3.2. Foredeep Deposition (Early to Middle Miocene)

The abrupt increase in accumulation rates and shift to chiefly fluvial and lacustrine facies reflect foreland basin advance and foredeep deposition in the Manantiales Basin by ~18 Ma (Figures 8a, 9b). The upward-coarsening stratigraphic packages are further compatible with episodic thrusting during eastward migration of the orogenic load (Figure 3; Perez, 1995; Jordan et al., 1996; Cristallini & Ramos, 2000; Pinto et al., 2018). Zircon U-Pb ages and gravel clast counts confirm sediment derivation from the Principal Cordillera, and potentially Cordillera de Santa Cruz in the central Frontal Cordillera, throughout the first and second upward-coarsening packages (Figure 3; Perez, 1995; Pérez, 2001). Simultaneous reduction of
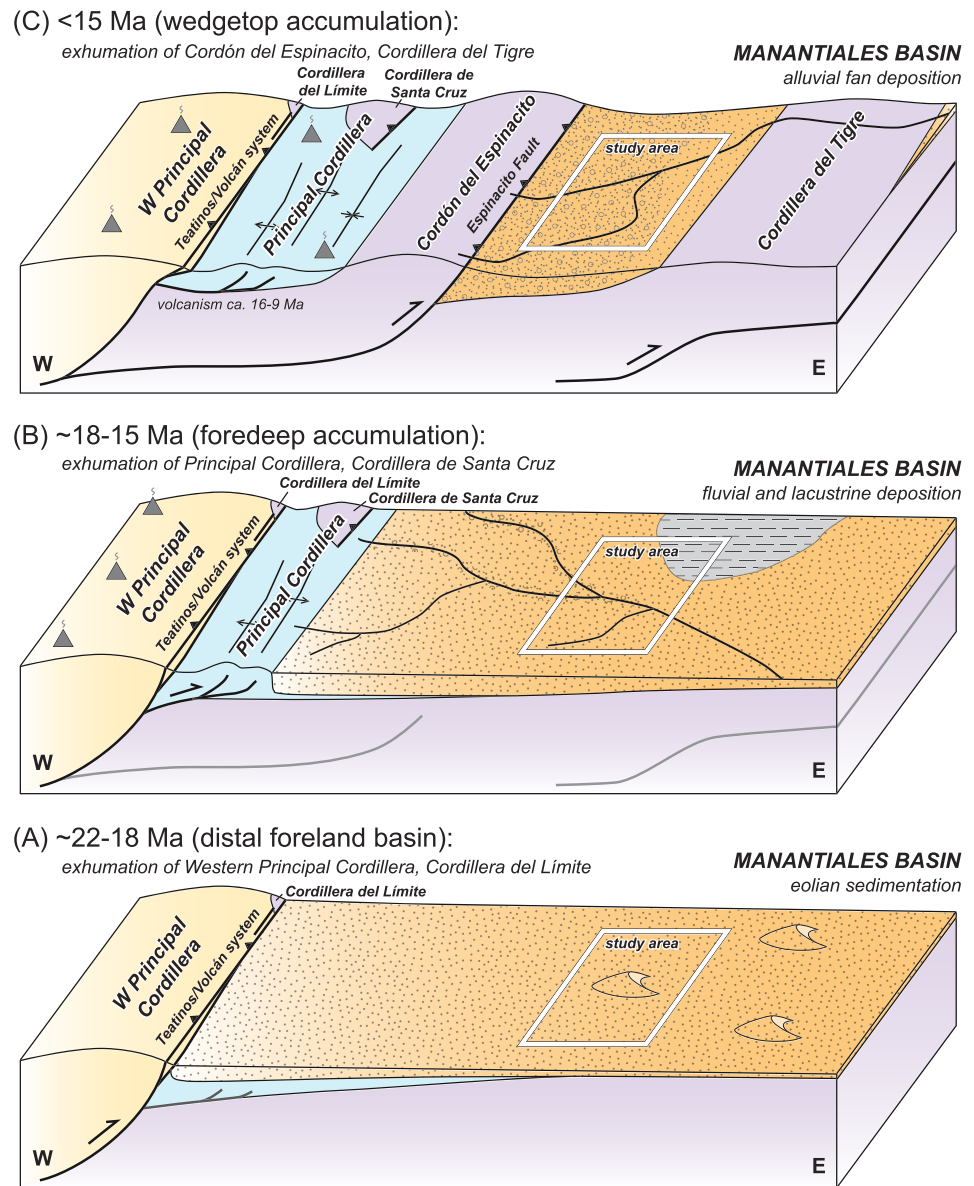
Fig 9. Schematic block diagrams illustrating hinterland deformation and Manantiales foreland basin evolution at ~32°S.

the Western Principal Cordillera detrital signal suggests inhibited sediment transport due to thrust migration and drainage reorganization (Figure 9b).

The shift to fluvial depositional systems occurred asynchronously throughout the retroarc region (~18 Ma in the Manantiales depocenter vs. 17–16 Ma in the Precordillera and Cacheuta basins, Figures 10a, 10b), consistent with south- and eastward migration of the foreland basin system. The establishment of braided rivers in western basin segments and distal fluvial-floodplain environments to the east is additionally compatible with the distribution of proximal-distal facies across a contiguous foredeep by ~17–16 Ma (Buelow et al., 2018; Levina et al., 2014). Though accumulation rates increased dramatically in the proximal Manantiales Basin following the transition to fluvial deposition, slow accumulation rates persisted in the Precordillera and Cacheuta depocenters consistent with the relatively distal basin locations (Figures 10a, 10b).

As observed in the Manantiales Basin, foredeep strata for the Precordillera and Cacheuta basins show diminished Western Principal Cordillera components and increased late Paleozoic–Triassic age signatures, with upsection trends toward younger late Paleozoic–Triassic detrital zircon age peaks (Bercowski et al., 1993;
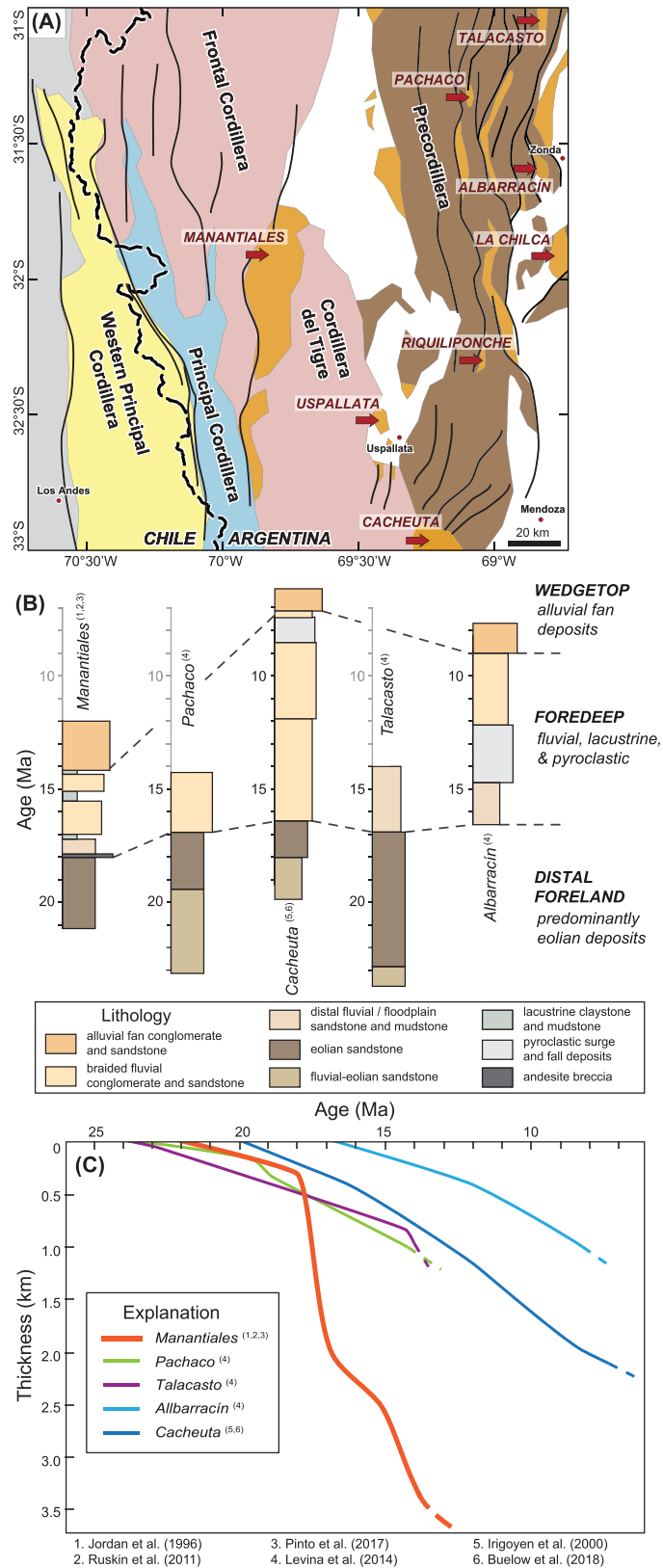
Fig 10. (a) Map above the modern Chile-Argentina flat slab subduction segment highlighting Neogene basin locations (indicated by red arrows). (b) Facies association diagram for Neogene synorogenic deposits. (c) Stratigraphic age versus thickness plot showing sediment accumulation histories for the Manantiales, Cacheuta, Pachaco, Talacasto, and Albarracín Basins.

Buelow et al., 2018; Jordan et al., 1993, 1996; Levina et al., 2014). Though Levina et al. (2014) interpreted the late Paleozoic–Triassic age shift to out-of-sequence deformation and exhumation of younger Choiyoi Group units in the hinterland, the decreased Western Principal Cordillera age signatures and regional upward-coarsening facies patterns match predicted trends during eastward thrust propagation. We alternatively suggest that the late Paleozoic–Triassic components in the Precordillera foredeep deposits reflect in-sequence exhumation of the same Principal Cordillera and Cordillera de Santa Cruz sources interpreted for the Manantiales Basin (Figure 9b).

Provenance results for the Albarracín, Cacheuta, and Pachaco basins also reflect the upsection introduction of clasts and detrital zircon age components indicative of Paleozoic sources in the Precordillera (Buelow et al., 2018; Levina et al., 2014). Given corollary facies and provenance evidence for an integrated foredeep depocenter during the early to middle Miocene, these components may indicate (1) initial exhumation of the western Precordillera preceding foreland basin partitioning and/or (2) exhumation of equivalent Paleozoic metasedimentary and sedimentary rocks exposed in the easternmost Frontal Cordillera at ~33°S (Buelow et al., 2018; Hoke et al., 2014; Levina et al., 2014; Suriano et al., 2017).

7.3.3. Wedge-Top Deposition and Basin Partitioning (Middle Miocene to Pliocene)

In the Manantiales Basin, facies and provenance trends from the third and fourth upward-coarsening packages recorded continued thrust belt migration, drainage reorganization, and foreland basin recycling (Figure 3). The transition to alluvial fan facies, close MDS provenance association with the Cordón del Espinacito, and introduction of rhyolite blocks in the upper boulder conglomerates strongly indicate exhumation of the Cordón del Espinacito and development of a significant topographic barrier along the western basin margin (Figure 8b; Jordan et al., 1996; Pérez, 2001). We interpret the third stratigraphic package to represent the transition from foredeep to wedge-top environments during initial shortening-induced exhumation and foreland basin recycling along the Espinacito fault. Establishment of the alluvial fan system in the uppermost package reflects sustained Espinacito fault motion, principal uplift of the Cordón del Espinacito, and well-developed wedge-top accumulation by ~14 Ma (Figure 9c). AHe cooling ages from the Eastern Principal Cordillera are compatible with shortening-induced exhumation of the Cordón del Espinacito from mainly 14 to 5 Ma, consistent with the foreland basin record. AHe results for the Manantiales deposits and piggyback basin analyses in the Uspallata depocenter suggest nearly contemporaneous exhumation of the Cordillera del Tigre at ~12–6.5 Ma (Figure 9c; Cortés, 1994; Hoke et al., 2014, 2015; Mahoney et al., 2014).

Minimum age constraints for the Pachaco and Talacasto depocenters indicate western Precordillera deformation and basin partitioning after ~14 Ma, compatible with the onset of major exhumation interpreted for the Cordón del Espinacito and Cordillera del Tigre and transition to wedge-top deposition in the Manantiales Basin (Figures 9c, 10b; Levina et al., 2014). By 12–9 Ma, AHe cooling ages and structural relationships in the Precordillera point to regionally synchronous, shortening-induced exhumation over >200 km across strike (Levina et al., 2014). The Cacheuta basin segment recorded continued foredeep deposition at ~12 Ma, followed by southward migration of the foreland basin system, recycling of subjacent strata, and wedge-top deposition at 8–7 Ma (Figures 10b, 10c; Buelow et al., 2018; Irigoyen et al., 2000). Uppermost synorogenic deposits throughout the hinterland and retroarc domains reflect late Miocene–Pliocene piggyback deposition (e.g., Beer et al., 1990; Cortés, 1994; Hoke et al., 2014; Mahoney et al., 2014; Ruskin & Jordan, 2007; Suriano et al., 2017).

Espinacito fault activity and piggyback basin accumulation continued from ~14 to potentially <5 Ma (Figure 9c; Hoke et al., 2015; Jordan et al., 1996; Pinto et al., 2018). Approximately 14−8 Ma AHe cooling ages from the Los Pelambres-Pachón region indicate synchronous cooling and tectonic exhumation in the hinterland, potentially triggered by middle Miocene thrusting along the Mondaquita fault (Figure 2; Maydagán et al., 2020). Crosscutting volcanic deposits and intrusions pin the cessation of major thin-skinned shortening in the Principal Cordillera before ~9 Ma, but broad-wavelength folds in the crosscutting volcanic units require minor late-stage hinterland deformation (Cristallini & Cangini, 1993). Our AHe results from the Western Principal Cordillera further suggest exhumational cooling during the late Miocene–Pliocene (~8–2.5 Ma). These AHe ages define a younger cooling episode than the results from Los Pelambres-Pachón but coincide with (1) a ~7 Ma AHe age obtained near the northern termination of the Pocuro fault (~45 km northwest of this study's sample locations); (2) thermal models that indicate ~7 Ma rapid cooling in the western Frontal Cordillera at 30°S; and (3) numerous ~8–2 Ma AHe and apatite
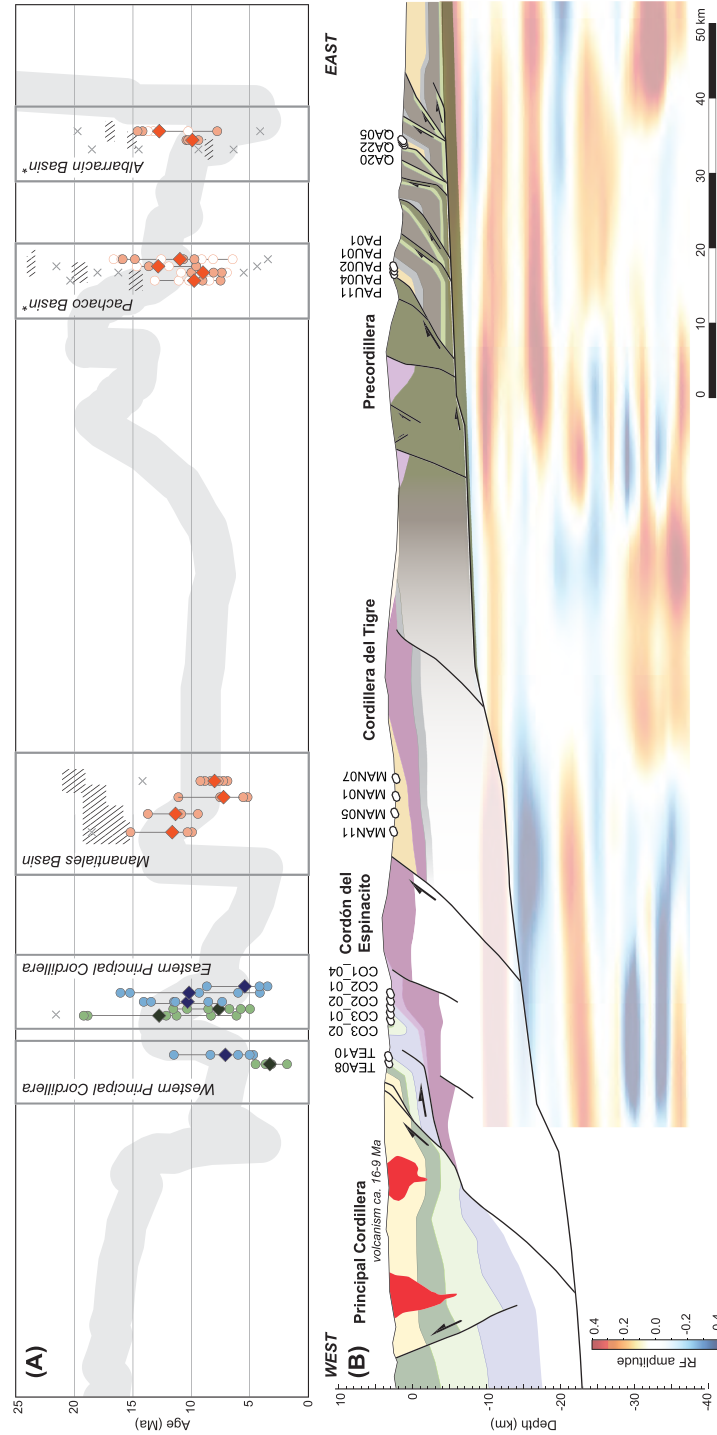
Fig 11. (a) Plot showing apatite (U-Th)/He cooling ages versus distance, from this study and Levina et al. (2014). Sample locations are shown in Figure 11b; symbols are explained in Figure 7. Orange datapoints correspond to Neogene basin samples; blue and green points reflect samples from Mesozoic sedimentary rocks in the Principal Cordillera. Thick gray line shows predicted apatite (U-Th)/He cooling ages for the representative cross section forward modeled in FetKin (supporting information Data Set S5). (b) Cross section of the study area (modified from Cristallini & Ramos, 2000; Jara & Charrier, 2014; Mpodozis et al., 2009; Rivano et al., 1993; Segemar, 2000; Sernageomin, 2003; von Gosen, 1992). Receiver function seismic data from Ammirati et al. (2016). Geologic units are explained in Figure 2.

fission track cooling ages from the Western Principal Cordillera at 33–35°S (Farías et al., 2008; Maksaev et al., 2009; McInnes et al., 2005; Piquer et al., 2017; Rodríguez et al., 2018). Regional late Miocene–Pliocene cooling ages consistently postdate the emplacement of magmatic or hydrothermal systems by at least several million years and point to a major episode of tectonic exhumation and surface uplift that affected the Andean hinterland from ~30°S to 35°S (Farías et al., 2008; Maksaev et al., 2009; Maydagán et al., 2020; Piquer et al., 2017; Rodríguez et al., 2018). At 32°S, seismicity beneath the hinterland and retroarc domains suggests contractional deformation is still active at depth (<10–20 km; Ammirati et al., 2015; Gregori & Christiansen, 2018; Marot et al., 2014).

7.4. Retroarc Structural Geometry at 32°S

In addition to providing insight into the timing of deformation-induced exhumation in active tectonic settings, low-temperature thermochronometry yields important information regarding the geometry of structures at depth. Focused exhumation along footwall ramps determines the location of the youngest reset thermochronometers, and previous studies have applied spatial patterns in cooling ages to refine nonemergent fault interpretations and deformation kinematics in mountain belts (e.g., Castelluccio et al., 2015; Lock & Willett, 2008; McQuarrie et al., 2008; McQuarrie & Ehlers, 2015, 2017; Mora et al., 2015; Reiners & Brandon, 2006). We combine regional structural, broadband seismic, and AHe data to investigate linkages between thin- and thick-skinned retroarc domains and explore the structural mechanisms controlling exhumational cooling at 32°S (Figure 11).

High-resolution local receiver function analyses corroborate the Precordillera décollement geometry determined from balanced cross sections (Figure 11b; Ammirati et al., 2016; Cristallini & Ramos, 2000; von Gosen, 1992). Based on the transition in positive arrival depths beneath the western Precordillera and Andean hinterland (from ~10 to 20 km) and previous interpretations of a change in detachment depth beneath the Precordillera and eastern Frontal Cordillera ranges (Cristallini & Ramos, 2000; Heredia et al., 2012), we propose a footwall ramp beneath the Cordillera del Tigre that links Precordillera faults with basement-involved structures to the west. AHe ages in the Western Principal Cordillera require another zone of focused exhumation in the hinterland. Given the overlap in cooling ages from the Western and Eastern Principal Cordilleras, high-amplitude positive arrivals beneath the Principal and Frontal Cordilleras at ~20-km depth, and supporting evidence for late Miocene–Pliocene uplift throughout the Andean retroarc, we consider a west dipping footwall ramp connected with the regional décollement (Figure 11; Ammirati et al., 2015, 2016; Cristallini & Ramos, 2000; Pérez, 2001). Minimum estimates of Neogene shortening in the Precordillera restore the transition from thin-skinned to basement-involved domains ~60–70 km to the west (beneath the modern Western Principal Cordillera; von Gosen, 1992), and if these shortening values are correct, the interpreted hinterland ramp may reflect a westward increase in décollement depth associated with the change in deformation styles (supporting information Table S5).

We use FetKin software (Finite Element Thermo-Kinematics; Almendral et al., 2015) to explore the viability of these structural interpretations. FetKin evaluates models of the thermal evolution from balanced cross sections by solving the transient advection-diffusion equation in two dimensions to compute time-temperature paths and predicted thermochronometric ages along a topographic profile. Misfits between the forward modeled ages and sample ages measured along the profile are reduced by iteratively adjusting FetKin inputs (including structural geometries/kinematics, deformational timing, and thermal parameters). A thermokinematic model is considered viable if forward modeled cooling ages reasonably match measured data (e.g., Almendral et al., 2015; Chapman et al., 2017; Mora et al., 2015).

A simplified balanced cross section based on published cross sections, regional geologic maps, and our nonemergent geometric interpretations effectively simulates the structures associated with exhumational cooling at 32°S (Figure 11b, S5). This cross section modifies Cristallini and Ramos (2000)'s orogen-scale reconstruction to include Frontal Cordillera structures from Heredia et al. (2002); revisions to the chronostratigraphy of the Western Principal Cordillera after Mpodozis et al. (2009), Jara and Charrier (2014), and Mackaman-Lofland et al. (2019); and minimum estimates of shortening and exhumation in the western Precordillera from Von Gosen (1992). Our decision to base western Precordillera interpretations after Von Gosen (1992) is further supported by (1) vitrinite reflectance data that suggest <5 km of burial reheating and exhumation in the western Precordillera since the Triassic, (2) alignment of the restored transition

from thin-skinned to basement-involved deformation with the west dipping ramp interpreted beneath the modern Western Principal Cordillera, and (3) well-documented evidence for pre-Andean deformation in this domain, including pre-Andean ductile fabrics and Ordovician–Devonian subcrop relationships for Carboniferous and Triassic deposits (Figure 2; Mpodozis & Ramos, 1990; Ragona et al., 1995; Urien et al., 2009; von Gosen, 1992).

The restored-state cross section was sequentially deformed to reproduce shortening in the Principal Cordillera, Frontal Cordillera, and Precordillera from 22 to 0 Ma, following the timing of deformation interpreted from the retroarc basin record and range of AHe ages measured along the profile (19.1 ± 1.1 to 3.6 ± 0.2 Ma). Final fault geometries, slip magnitudes, and topography were required to match the modern cross section illustrated in Figure 11b (Cristallini & Ramos, 2000; Heredia et al., 2002; Jara & Charrier, 2014; von Gosen, 1992). The timing and shortening magnitude for intermediate steps were iteratively adjusted to achieve the best fit between predicted and measured AHe cooling ages. Past topographic profiles were estimated assuming horizontal initial topography and focused erosion above active zones of fault-induced uplift (e.g., Table S5; Castelluccio et al., 2015). The resultant thermokinematic model remains inherently schematic (e.g., lithospheric flexure and topographic growth associated with the attainment of critical taper were not systematically incorporated into each deformation step; Rak et al., 2017; Robinson & McQuarrie, 2012), but the results provide an informative test of the structural mechanisms responsible for (1) zones of high-magnitude exhumation along the profile, (2) the positive AHe cooling age-stratigraphic level relationships in both the Manantiales Basin and Eastern Principal Cordillera, and (3) late-stage hinterland exhumation documented in the Western Principal Cordillera during the late Miocene-Pliocene.

We reiterate that samples collected from key structural locations along the Espinacito fault hanging wall and Cordillera del Tigre did not yield apatite suitable for analyses, limiting our comparison of predicted and measured cooling ages. However, a kinematic sequence that accommodates rapid regional deformation over the past 16 Myr provides an excellent match between forward modeled and available sample ages, and a final episode of shortening along the hinterland ramp and Espinacito fault system initiating at 5–2 Ma effectively fits the youngest measured AHe ages in the Western Principal Cordillera (Figure 11a, S5). Though alternative middle to upper crustal interpretations and deformation kinematics remain viable, FetKin model results are compatible with (1) initial exhumation of the Cordillera del Tigre and Manantiales Basin deposits along a hinterland ramp at the restored transition from thin-skinned to basement-involved structural styles and (2) rapid translation of the Principal Cordillera, Frontal Cordillera, and Manantiales domains along a hybrid thin- and thick-skinned regional décollement during high-magnitude shortening in the Precordillera. These interpretations provide viable mechanisms for Cordillera del Tigre uplift and Manantiales Basin exhumation given the lack of mapped contractional faults at the range margins. Model results also provide testable hypotheses for future work, including sampling of rock types along strike that may be more fertile in the minerals necessary for thermochronology.

8. Conclusions

1. New ^{40}Ar/^{39}Ar volcanic ages and detrital zircon maximum depositional ages constrain the timing of synorogenic clastic deposition in the retroarc Manantiales Basin. Basal eolian facies recorded initial subsidence and distal foreland basin accumulation from ~22 to 18 Ma. Upward-coarsening facies packages in overlying fluvial and lacustrine deposits reflect thrust motion, eastward (cratonward) migration of the flexural basin system, and medial to proximal foredeep deposition until ~15 Ma. Coarse alluvial fan facies point to wedge-top deposition by ~14 Ma, consistent with thermochronological controls on the timing of thrust propagation.

2. Manantiales Basin provenance results signify sequential unroofing along both thin-skinned and basement-involved thrust sheets in the Principal and Frontal Cordilleras. Detrital zircon U-Pb ages and published geochemical, detrital heavy mineral, and sandstone petrographic data sets indicate sediment contribution from the Western Principal Cordillera and Cordillera del Límite during shortening-induced exhumation along structures at the eastern domain margin (Teatinos/Volcán and related fault systems) from ~22 to 18 Ma. Substantial Principal and Frontal Cordillera detrital components introduced in overlying fluvial and lacustrine foredeep deposits reflect eastward advance of the thrust belt and exhumation of both the basement-involved Cordillera de Santa Cruz and

thin-skinned Principal Cordillera during accumulation of the first and second facies packages at ~18–15 Ma. Provenance associations indicate sediment recycling from Mesozoic and older Cenozoic basin units during initial exhumation along the thick-skinned Espinacito fault and accumulation of the third stratigraphic package (~15 Ma); shutoff of hinterland detrital signatures and introduction of rhyolite blocks in the upper Manantiales deposits require continued exhumation, uplift of the Cordón del Espinacito, and development of a significant topographic barrier by ~14 Ma.

3. Apatite (U-Th)/He (AHe) cooling ages confirm that the majority of shortening-induced exhumation along the Cordón del Espinacito and Cordillera del Tigre was nearly synchronous (from roughly ~14 to <5 Ma), consistent with the Manantiales Basin provenance record and upper facies transition. Late Miocene–Pliocene (~8–2.5 Ma) AHe ages in the Western Principal Cordillera are younger than crosscutting volcanic units that pin the timing of thin-skinned deformation and are compatible with exhumational cooling along nonemergent hinterland structures during late-stage orogenesis.

4. Updated chronostratigraphic and provenance correlations between the Manantiales Basin and coeval basin segments in the Precordillera and modern foreland reveal south- and eastward migration of a contiguous foreland basin system from ~20 to 14 Ma, followed by partitioning of western (proximal) basin segments during Cordillera del Tigre and western Precordillera deformation at ~14 Ma. Provenance data sets for these Neogene deposits show patterns of sequential hinterland exhumation compatible with Manantiales Basin results, punctuated by locally significant contributions from syndepositional volcanic centers.

5. By ~12–9 Ma, thermochronometric and provenance results for hinterland and Precordillera basin deposits indicate regionally synchronous shortening, foreland basin recycling, and exhumational cooling during rapid development of the Precordillera thrust belt. Deformation throughout the hinterland and retroarc domains persisted until at least the late Miocene–Pliocene.

6. Integrated structural, thermochronological, and geophysical data sets are compatible with rapid exhumation of the Principal Cordillera, Frontal Cordillera, and Manantiales Basin deposits along a regionally connected, hybrid thin- and thick-skinned décollement.

REFERENCES

Alarcón, P., & Pinto, L. (2015). Neogene erosion of the Andean Cordillera in the flat-slab segment as indicated by petrography and whole-rock geochemistry from the Manantiales Foreland Basin (32°–32°30′S). *Tectonophysics*, *639*, 1–22. https://doi.org/10.1016/j.tecto.2014.11.001

Allmendinger, R. W., Figueroa, D., Snyder, D., Beer, J., Mpodozis, C., & Isacks, B. L. (1990). Foreland shortening and crustal balancing in the Andes at 30°S latitude. *Tectonics*, *9*(4), 789–809. https://doi.org/10.1029/TC009i004p00789

Allmendinger, R. W., & Judge, P. A. (2014). The Argentine Precordillera: A foreland thrust belt proximal to the subducted plate. *Geosphere*, *10*(6), 1203–1218. https://doi.org/10.1130/GES01062.1

Almendral, A., Robles, W., Parra, M., Mora, A., Ketcham, R. A., & Raghib, M. (2015). FetKin: Coupling kinematic restorations and temperature to predict thrusting, exhumation histories, and thermochronometric ages. *AAPG Bulletin*, *99*(8), 1557–1573. https://doi.org/10.1306/07071411112

Alvarado, P., Beck, S., & Zandt, G. (2007). Crustal structure of the south-Central Andes Cordillera and backarc region from regional waveform modelling. *Geophysical Journal International*, *170*(2), 858–875. https://doi.org/10.1111/j.1365-246X.2007.03452.x

Álvarez, J., Mpodozis, C., Arriagada, C., Astini, R., Morata, D., Salazar, E., et al. (2011). Detrital zircons from late Paleozoic accretionary complexes in north-central Chile (28°–32°S): Possible fingerprints of the Chilenia terrane. *Journal of South American Earth Sciences*, *34*(4), 460–476. https://doi.org/10.1016/j.jsames.2011.06.002

Ammirati, J. B., Alvarado, P., & Beck, S. (2015). A lithospheric velocity model for the flat slab region of Argentina from joint inversion of Rayleigh wave phase velocity dispersion and teleseismic receiver functions. *Geophysical Journal International*, *202*(1), 224–241. https://doi.org/10.1093/gji/ggv140

Ammirati, J. B., Alvarado, P., Perarnau, M., Saez, M., & Monsalvo, G. (2013). Crustal structure of the Central Precordillera of San Juan, Argentina (31°S) using teleseismic receiver functions. *Journal of South American Earth Sciences*, *46*, 100–109. https://doi.org/10.1016/j.jsames.2013.05.007

Ammirati, J. B., Pérez Luján, S., Alvarado, P., Beck, S., Rocher, S., & Zandt, G. (2016). High-resolution images above the Pampean flat slab of Argentina (31–32°S) from local receiver functions: Implications on regional tectonics. *Earth and Planetary Science Letters*, *450*, 29–39. https://doi.org/10.1016/j.epsl.2016.06.018

Anderson, R. B., Long, S. P., Horton, B. K., Calle, A. Z., & Ramirez, V. (2017). Shortening and structural architecture of the Andean fold-thrust belt of southern Bolivia (21°S): Implications for kinematic development and crustal thickening of the Central Andes. *Geosphere*, *13*(2), 538–558. https://doi.org/10.1130/GES01433.1

Beer, J. A., Allmendinger, R. W., Figueroa, D. E., & Jordan, T. E. (1990). Seismic stratigraphy of a Neogene piggyback basin, Argentina. *AAPG Bulletin*, *74*(8), 1183–1202.

Bercowski, F., Ruzycki, L., Jordan, T., Zeitler, P., Caballero, M. M., & Perez, I. (1993). Litofacies y edad isotópica de la secuencia La Chilca y su significado paleogeográfico para el Neógeno de Precordillera. In *12th Congreso Geológico Argentino and 2nd Congreso de Exploración de Hidrocarburos, Proceedings T°1* (pp. 212–217). Buenos Aires.

Boyce, J. W., & Hodges, K. V. (2005). U and Th zoning in Cerro de Mercado (Durango, Mexico) fluorapatite: Insights regarding the impact of recoil redistribution of radiogenic 4He on (U-Th)/He thermochronology. *Chemical Geology*, *219*(1-4), 261–274. https://doi.org/10.1016/j.chemgeo.2005.02.007

Buelow, E. K., Suriano, J., Mahoney, J. B., Kimbrough, D. L., Mescua, J. F., Giambiagi, L. B., & Hoke, G. D. (2018). Sedimentologic and stratigraphic evolution of the Cacheuta basin: Constraints on the development of the Miocene retroarc foreland basin, south-Central Andes. *Lithosphere*, *10*(3), 366–391. https://doi.org/10.1130/l709.1

Capaldi, T. N., Horton, B. K., McKenzie, N. R., Stockli, D. F., & Odlum, M. L. (2017). Sediment provenance in contractional orogens: The detrital zircon record from modern rivers in the Andean fold-thrust belt and foreland basin of western Argentina. *Earth and Planetary Science Letters*, *479*, 83–97. https://doi.org/10.1016/j.epsl.2017.09.001

Carretier, S., Tolorza, V., Rodríguez, M. P., Pepin, E., Aguilar, G., Regard, V., et al. (2015). Erosion in the Chilean Andes between 27°S and 39°S: Tectonic, climatic and geomorphic control. *Geological Society, London, Special Publications*, *399*(1), 401–418. https://doi.org/10.1144/SP399.16

Castelluccio, A., Andreucci, B., Zattin, M., Ketcham, R. A., Jankowski, L., Mazzoli, S., & Szaniawski, R. (2015). Coupling sequential restoration of balanced cross sections and low-temperature thermochronometry: The case study of the Western Carpathians. *Lithosphere*, *7*(4), 367–378. https://doi.org/10.1130/L436.1

Chapman, J. B., Carrapa, B., Ballato, P., DeCelles, P. G., Worthington, J., Oimahmadov, I., et al. (2017). Intracontinental subduction beneath the Pamir Mountains: Constraints from thermokinematic modeling of shortening in the Tajik fold-and-thrust belt. *GSA Bulletin*, *129*(11-12), 1450–1471. https://doi.org/10.1130/B31730.1

Charrier, R., Baeza, O., Elgueta, S., Flynn, J. J., Gans, P., Kay, S. M., et al. (2002). Evidence for Cenozoic extensional basin development and tectonic inversion south of the flat-slab segment, southern Central Andes, Chile (33°-36°S.L.). *Journal of South American Earth Sciences*, *15*(1), 117–139. https://doi.org/10.1016/S0895-9811(02)00009-3

Charrier, R., Pinto, L., & Rodríguez, M. (2007). Tectonostratigraphic evolution of the Andean orogen in Chile. In G. W. Moreno T (Ed.), *The Geology of Chile* (pp. 21–114). London: Geoloical Society of London.

Charrier, R., Ramos, V. A., Tapia, F., & Sagripanti, L. (2015). Tectono-stratigraphic evolution of the Andean Orogen between 31 and 37°S (Chile and Western Argentina). *Geological Society, London, Special Publications*, *399*(1), 13–61. https://doi.org/10.1144/SP399.20

Cortés, J. (1994). La segmentación tectónica de la Depresión de Uspallata, Mendoza, Argentina. In *7th Congreso Geológico Argentino 1. Proceedings*, (pp. 18–22). Concepción, Chile_: 7th Congreso Geológico Argentino.

Cristallini, E. O., & Cangini, A. (1993). Estratigrafía y estructura de las nacientes del Río Volcán, Alta Cordillera de San Juan. In *Congreso Geológico Argentino no. 12*, (pp. 85–92). Buenos Aires, Argentina.

Cristallini, E. O., & Ramos, V. A. (2000). Thick-skinned and thin-skinned thrusting in the La Ramada fold and thrust belt: Crustal evolution of the High Andes of San Juan, Argentina (32°SL). *Tectonophysics, 317*(3-4), 205-235. https://doi.org/10.1016/S0040-1951(99)00276-0

Dahlquist, J. A., Alasino, P. H., Basei, M. A. S., Morales Cámera, M. M., Macchioli Grande, M., & da Costa Campos Neto, M. (2018). Petrological, geochemical, isotopic, and geochronological constraints for the Late Devonian–Early Carboniferous magmatism in SW Gondwana (27–32°LS): An example of geodynamic switching. *International Journal of Earth Sciences*, *107*(7), 2575–2603. https://doi.org/10.1007/s00531-018-1615-9

DeCelles, P. G. (2012). Foreland basin systems revisited: Variations in response to rectonic settings. In *Tectonics of Sedimentary Basins: Recent Advances* (pp. 405–426). Hoboken, New Jersey, USA: Blackwell Publishing Ltd. https://doi.org/10.1002/9781444347166.ch20

DeCelles, P. G., & Giles, K. A. (1996). Foreland basin systems. *Basin Research*, *8*(2), 105–123. https://doi.org/10.1046/j.1365-2117.1996.01491.x

DeCelles, P. G., & Horton, B. K. (2003). Early to middle Tertiary foreland basin development and the history of Andean crustal shortening in Bolivia. *Geological Society of America Bulletin, 115*(1), 58-77. https://doi.org/10.1130/0016-7606(2003)115<0058:ETMTFB>2.0.CO;2

Dewey, J. F. (1980). Episodicity, sequence and style at convergent plate boundaries. *The continental crust and its mineral deposits*, (20), 553–573.

Ehlers, T. A., & Farley, K. A. (2003). Apatite (U-Th)/He thermochronometry: Methods and applications to problems in tectonic and surface processes. *Earth and Planetary Science Letters, 206*(1-2), 1-14. https://doi.org/10.1016/S0012-821X(02)01069-5

Farías, M., Charrier, R., Carretier, S., Martinod, J., Fock, A., Campbell, D., et al. (2008). Late Miocene high and rapid surface uplift and its erosional response in the Andes of central Chile (33°–35°S). *Tectonics*, *27*(1), n/a. https://doi.org/10.1029/2006TC002046

Farías, M., Comte, D., Charrier, R., Martinod, J., David, C., Tassara, A., et al. (2010). Crustal-scale structural architecture in central Chile based on seismicity and surface geology: Implications for Andean mountain building. *Tectonics*, *29*(3). https://doi.org/10.1029/2009TC002480

Farley, K. A., & Stockli, D. F. (2002). (U-Th)/He dating of phosphates: Apatite, monazite, and xenotime. *Reviews in Mineralogy and Geochemistry*, *48*(1), 559–577. https://doi.org/10.2138/rmg.2002.48.15

Finney, S., Peralta, S., Gehrels, G., & Marsaglia, K. (2005). The Early Paleozoic history of the Cuyania (greater Precordillera) terrane of western Argentina: Evidence from geochronology of detrital zircons from Middle Cambrian sandstones. *Geologica Acta*, *3*(4), 339–354.

Flowers, R. M., Ketcham, R. A., Shuster, D. L., & Farley, K. A. (2009). Apatite (U-Th)/He thermochronometry using a radiation damage accumulation and annealing model. *Geochimica et Cosmochimica Acta*, *73*(8), 2347–2365. https://doi.org/10.1016/j.gca.2009.01.015

Fosdick, J. C., Reat, E. J., Carrapa, B., Ortiz, G., & Alvarado, P. M. (2017). Retroarc basin reorganization and aridification during Paleogene uplift of the southern Central Andes. *Tectonics*, *36*(3), 493–514. https://doi.org/10.1002/2016TC004400

Gans, C. R., Beck, S. L., Zandt, G., Gilbert, H., Alvarado, P., Anderson, M., & Linkimer, L. (2011). Continental and oceanic crustal structure of the Pampean flat slab region, western Argentina, using receiver function analysis: New high-resolution results. *Geophysical Journal International*, *186*(1), 45–58. https://doi.org/10.1111/j.1365-246X.2011.05023.x

Giambiagi, L., Mescua, J., Bechis, F., Tassara, A., & Hoke, G. (2012). Thrust belts of the southern Central Andes: Along-strike variations in shortening, topography, crustal geometry, and denudation. *Geological Society of America Bulletin*, *124*(7-8), 1339–1351. https://doi.org/10.1130/B30609.1

Gleason, J. D., Finney, S. C., Peralta, S. H., Gehrels, G. E., & Marsaglia, K. M. (2007). Zircon and whole-rock Nd-Pb isotopic provenance of Middle and Upper Ordovician siliciclastic rocks, Argentine Precordillera. *Sedimentology*, *54*(1), 107–136. https://doi.org/10.1111/j.1365-3091.2006.00820.x

Gregori, S. D., & Christiansen, R. (2018). Seismic hazard analysis for central-western Argentina. *Geodesy and Geodynamics*, *9*(1), 25–33. https://doi.org/10.1016/j.geog.2017.07.006

Harrison, T. M. (1982). Diffusion of 40 Ar in hornblende. *Contributions to Mineralogy and Petrology*, *78*(3), 324–331.

Hart, N. R., Stockli, D. F., & Hayman, N. W. (2016). Provenance evolution during progressive rifting and hyperextension using bedrock and detrital zircon U-Pb geochronology, Mauléon Basin, western Pyrenees. *Geosphere*, *12*(4), 1166–1186. https://doi.org/10.1130/GES01273.1

Heredia, N., Farias, P., García-Sansegundo, J., & Giambiagi, L. (2012). The basement of the Andean Frontal Cordillera in the Cordón del Plata (Mendoza, Argentina): Geodynamic evolution. *Andean Geology*, *39*(2), 242–257. https://doi.org/10.5027/andgeov39n2-a03

Heredia, N., Rodríguez Fernández, L. R., Gallastegui, G., Busquets, P., & Colombo, F. (2002). Geological setting of the Argentine Frontal Cordillera in the flat-slab segment (30°00′–31°30′S latitude). *Journal of South American Earth Sciences*, *15*(1), 79–99. https://doi.org/10.1016/S0895-9811(02)00007-X

Hervé, F., Calderón, M., Fanning, C. M., Pankhurst, R. J., & Godoy, E. (2013). Provenance variations in the Late Paleozoic accretionary complex of central Chile as indicated by detrital zircons. *Gondwana Research*, *23*(3), 1122–1135. https://doi.org/10.1016/j.gr.2012.06.016

Hervé, F., Fanning, C. M., Calderón, M., & Mpodozis, C. (2014). Early Permian to Late Triassic batholiths of the Chilean Frontal Cordillera (28°–31°S): SHRIMP U-Pb zircon ages and Lu-Hf and O isotope systematics. *Lithos*, *184*, 436–446. https://doi.org/10.1016/j.lithos.2013.10.018

Hoke, G. D., Giambiagi, L. B., Garzione, C. N., Mahoney, J. B., & Strecker, M. R. (2014). Neogene paleoelevation of intermontane basins in a narrow, compressional mountain range, southern Central Andes of Argentina. *Earth and Planetary Science Letters*, *406*, 153–164. https://doi.org/10.1016/j.epsl.2014.08.032

Hoke, G. D., Graber, N. R., Mescua, J. F., Giambiagi, L. B., Fitzgerald, P. G., & Metcalf, J. R. (2015). Near pure surface uplift of the Argentine Frontal Cordillera: Insights from (U–Th)/He thermochronometry and geomorphic analysis. *Geological Society, London, Special Publications*, *399*(1), 383–399. https://doi.org/10.1144/sp399.4

Horton, B. K. (2018a). Sedimentary record of Andean mountain building. *Earth-Science Reviews*, *178*, 279–309. https://doi.org/10.1016/j.earscirev.2017.11.025

Horton, B. K. (2018b). Tectonic regimes of the Central and Southern Andes: Responses to variations in plate coupling during subduction. *Tectonics*, *37*, 402–429. https://doi.org/10.1002/2017TC004624

Horton, B. K., & Decelles, P. G. (2001). Modern and ancient fluvial megafans in the foreland basin system of the Central Andes, southern Bolivia: Implications for drainage network evolution in fold-thrust belts. *Basin Research*, *13*(1), 43–63. https://doi.org/10.1046/j.1365-2117.2001.00137.x

Horton, B. K., Fuentes, F., Boll, A., Starck, D., Ramirez, S. G., & Stockli, D. F. (2016). Andean stratigraphic record of the transition from backarc extension to orogenic shortening: A case study from the northern Neuquén Basin, Argentina. *Journal of South American Earth Sciences*, *71*, 17–40. https://doi.org/10.1016/j.jsames.2016.06.003

Huntington, K. W., Ehlers, T. A., Hodges, K. V., & Whipp, D. M. Jr. (2007). Topography, exhumation pathway, age uncertainties, and the interpretation of thermochronometer data. *Tectonics*, *26*(4). https://doi.org/10.1029/2007TC002108

Iglesia Llanos, M. P. (1995). Geología del área de Manantiales al este del Cordón del Espinacito, Provincia de San Juan. *Revista del la Asociación Geológica Argentina*, *50*(1–4), 195–211.

Irigoyen, M. V., Buchan, K. L., & Brown, R. L. (2000). Magnetostratigraphy of Neogene Andean foreland-basin strata, lat 33°S, Mendoza Province, Argentina. *Geological Society of America Bulletin*, *112*(6), 803–816. https://doi.org/10.1130/0016-7606(2000)112<803:MONAFS>2.0.CO;2

Isacks, B. L. (1988). Uplift of the central Andean plateau and bending of the Bolivian orocline. *Journal of Geophysical Research: Solid Earth*, *98*(B4), 3211–3231. https://doi.org/10.1029/JB093iB04p03211

Jackson, S. E., Pearson, N. J., Griffin, W. L., & Belousova, E. A. (2004). The application of laser ablation-inductively coupled plasma-mass spectrometry to in situ U-Pb zircon geochronology. *Chemical Geology*, *211*(1-2), 47–69. https://doi.org/10.1016/j.chemgeo.2004.06.017

Jara, P., & Charrier, R. (2014). Nuevos antecedentes estratigráficos y geocronológicos para el Meso-Cenozoico de la Cordillera Principal de Chile entre 32° y 32°30′S: Implicancias estructurales y paleogeográficas. *Andean Geology*, *41*(1), 174–209. https://doi.org/10.5027/andgeoV41n1-a07

Jordan, T. E. (1995). Retroarc foreland and related basins. In *Tectonics of Sedimentary Basins* (pp. 331–391). Hoboken, New Jersey, USA: Blackwell Publishing Ltd.

Jordan, T. E., Allmendinger, R. W., Damanti, J. F., & Drake, R. E. (1993). Chronology of motion in a complete thrust belt: The Precordillera, 30′31°S, Andes Mountains. *The Journal of Geology*, *101*(2), 135–156. https://doi.org/10.1086/648213

Jordan, T. E., Schlunegger, F., & Cardozo, N. (2001). Unsteady and spatially variable evolution of the Neogene Andean Bermejo foreland basin, Argentina. *Journal of South American Earth Sciences*, *14*(7), 775–798. https://doi.org/10.1016/S0895-9811(01)00072-4

Jordan, T. E., Tamm, V., Figueroa, G., Flemings, P. B., Richards, D., Tabbutt, K., & Cheatham, T. (1996). Development of the Miocene Manantiales foreland basin, Principal Cordillera, San Juan, Argentina. *Andean Geology*, *23*(1), 43–79.

Kay, S. M., & Mpodozis, C. (2002). Magmatism as a probe to the Neogene shallowing of the Nazca plate beneath the modern Chilean flat-slabs. *Journal of South American Earth Sciences*, *15*(1), 39–57. https://doi.org/10.1016/S0895-9811(02)00005-6

Kleiman, L. E., & Japas, M. S. (2009). The Choiyoi volcanic province at 34°S–36°S (San Rafael, Mendoza, Argentina): Implications for the Late Palaeozoic evolution of the southwestern margin of Gondwana. *Tectonophysics*, *473*(3–4), 283–299. https://doi.org/10.1016/j.tecto.2009.02.046

Kley, J. (1996). Transition from basement-involved to thin-skinned thrusting in the Cordillera Oriental of southern Bolivia. *Tectonics*, *15*(4), 763–775. https://doi.org/10.1029/95TC03868

Kley, J., & Monaldi, C. R. (1998). Tectonic shortening and crustal thickness in the Central Andes: How good is the correlation? *Geology*, *26*(8), 723–726. https://doi.org/10.1130/0091-7613(1998)026<0723:TSACTI>2.3.CO;2

Kooi, H., & Beaumont, C. (1996). Large-scale geomorphology: Classical concepts reconciled and integrated with contemporary ideas via a surface processes model. *Journal of Geophysical Research: Solid Earth*, *101*(B2), 3361–3386. https://doi.org/10.1029/95JB01861

Kuiper, K. F., Deino, A., Hilgen, F. J., Krijgsman, W., Renne, P. R., & Wijbrans, A. J. (2008). Synchronizing rock clocks of Earth history. *Science*, *320*, 500–504. https://doi.org/10.1126/science.1154339

Leveratto, M. A. (1976). Edad de intrusivos Cenozoicos en la Precordillera de San Juan y su implicancia estratigráfica. *Revista de La Asociación Geológica Argentina*, *31*(1), 53–58.

Levina, M., Horton, B. K., Fuentes, F., & Stockli, D. F. (2014). Cenozoic sedimentation and exhumation of the foreland basin system preserved in the Precordillera thrust belt (31–32°S), southern Central Andes, Argentina. *Tectonics*, *33*(9), 1659–1680. https://doi.org/10.1002/2013TC003424

Lock, J., & Willett, S. (2008). Low-temperature thermochronometric ages in fold-and-thrust belts. *Tectonophysics*, *456*(3-4), 147–162. https://doi.org/10.1016/j.tecto.2008.03.007

López, G. M., Vucetich, M. G., Carlini, A. A., Bond, M., Pérez, M. E., Ciancio, M. R., et al. (2011). New Miocene mammal assemblages from Neogene Manantiales basin, Cordillera Frontal, San Juan, Argentina. In J. A. Salfity, & R. A. Marquilas (Eds.), *Cenozoic Geology of the Central Andes of Argentina*, (pp. 211, 978-987-26890-0-1–226). Salta: SCS Publisher.

Lossada, A. C., Giambiagi, L., Hoke, G. D., Fitzgerald, P. G., Creixell, C., Murillo, I., et al. (2017). Thermochronologic evidence for late Eocene Andean mountain building at 30°S. *Tectonics*, *36*(11), 2693–2713. https://doi.org/10.1002/2017TC004674

Mackaman-Lofland, C., Horton, B. K., Fuentes, F., Constenius, K. N., & Stockli, D. F. (2019). Mesozoic to Cenozoic retroarc basin evolution during changes in tectonic regime, southern Central Andes (31–33°S): Insights from zircon U-Pb geochronology. *Journal of South American Earth Sciences*, *89*, 299–318. https://doi.org/10.1016/j.jsames.2018.10.004

Mahoney, J. B., Kimbrough, D., Hoke, G., Mescua, J., Giambiagi, L., Buelow, E., et al. (2014). *Cuenca Uspallata: An intermontane basin records episodic uplift of the Cordillera Frontal and Precordillera in the late Miocene*, In *Geological Society of America Meeting* (Poster N°143-8). Vancouver, Canada: Geological Society of America.

Maksaev, V., Munizaga, F., & Tassinari, C. (2014). Timing of the magmatism of the paleo-Pacific border of Gondwana: U-Pb geochronology of Late Paelozoic to Early Mesozoic igneous rocks of the north Chilean Andes between 20° and 31°S. *Andean Geology*, *41*(3), 447–506. https://doi.org/10.5027/andgeoV41n3-a01

Maksaev, V., Munizaga, F., Zentilli, M., & Charrier, R. (2009). Fission track thermochronology of Neogene plutons in the Principal Andean Cordillera of central Chile (33–35°S): Implications for tectonic evolution and porphyry Cu-Mo mineralization. *Andean Geology*, *36*(2), 153–171. http://www.redalyc.org/articulo.oa?id=173914378001

Marot, M., Monfret, T., Gerbault, M., Nolet, G., Ranalli, G., & Pardo, M. (2014). Flat versus normal subduction zones: A comparison based on 3-D regional traveltime tomography and petrological modelling of central Chile and western Argentina (29°–35°S). *Geophysical Journal International*, *199*(3), 1633–1654. https://doi.org/10.1093/gji/ggu355

Maydagán, L., Zattin, M., Mpodozis, C., Selby, D., Franchini, M., & Dimieri, L. (2020). Apatite (U–Th)/He thermochronology and Re–Os ages in the Altar region, Central Andes of San Juan (31°30′S), Main Cordillera of San Juan, Argentina: implications of rapid exhumation in the porphyry Cu (Au) metal endowment and regional tectonics. *Mineralium Deposita*, 1–20.

McInnes, B. I., Evans, N. J., Fu, F. Q., Garwin, S., Belousova, E., Griffin, W. L., W.L., et al. (2005). *Thermal history analysis of selected Chilean, Indonesian, and Iranian porphyry Cu-Mo-Au deposits. Super porphyry copper and gold deposits: A global perspective (Porter, TM; editor)*. Porter Geoconsultancy Publishing, de Adelaide, Australia, 27-42.

McQuarrie, N. (2002). Initial plate geometry, shortening variations, and evolution of the Bolivian orocline. *Geology*, *30*(10), 867–870. https://doi.org/10.1130/0091-7613(2002)030<0867:IPGSVA>2.0.CO;2

McQuarrie, N., Barnes, J. B., & Ehlers, T. A. (2008). Geometric, kinematic, and erosionalhistory of the central Andean Plateau, Bolivia (15–17°S). *Tectonics*, *27*(3). https://doi.org/10.1029/2006TC002054

McQuarrie, N., & Ehlers, T. A. (2015). Influence of thrust belt geometry and shortening rate on thermochronometer cooling ages: Insights from thermokinematic and erosion modeling of the Bhutan Himalaya. *Tectonics*, *34*(6), 1055–1079. https://doi.org/10.1002/2014TC003783

McQuarrie, N., & Ehlers, T. A. (2017). Techniques for understanding fold-and-thrust belt kinematics and thermal evolution. In R. D. Law, J. R. Thigpen, A. J. Merschat, & H. H. Stowell (Eds.), *Linkages and Feedbacks in Orogenic Systems, GSA Memoirs* (pp. 25–54). Boulder, Colorado, USA: The Geological Society of America. https://doi.org/10.1130/2017.1213(02

Mirré, J. (1966). Geología del valle del Río de Los Patos (entre Barreal y Las Hornillas). *Revista de La Asociación Geológica Argentina*, *21*(4), 211–231.

Mora, A., Casallas, W., Ketcham, R. A., Gomez, D., Parra, M., Namson, J., et al. (2015). Kinematic restoration of contractional basement structures using thermokinematic models: A key tool for petroleum system modeling. *AAPG Bulletin*, *99*(8), 1575–1598. https://doi.org/10.1306/04281411108

Mpodozis, C., Brockway, H., Marquardt, C., & Perelló, J. (2009). Geocronología U/Pb y tectónica de la región de Los Pelambres-Cerro Mercedario: Implicancias para la evolución cenozoica de los Andes del centro de Chile y Argentina. *Congreso Geológico Chileno*, *12*(S9_059).

Mpodozis, C., & Kay, S. M. (1992). Late Paleozoic to Triassic evolution of the Gondwana margin: Evidence from Chilean Frontal Cordilleran batholiths (28°S to 31°S). *Geological Society of America Bulletin*, *104*(8), 999–1014. https://doi.org/10.1130/0016-7606(1992)104<0999:LPTTEO>2.3.CO;2

Mpodozis, C., & Ramos, V. A. (1990). The Andes of Chile and Argentina. In G. E. Ericksen, M. T. Canas Pinochet, & J. A. Reinemund (Eds.), *Geology of the Andes and its relation to hydrocarbon and mineral resources*, (pp. 59–90). Houston, TX: Circum-Pacific Council for Energy and Mineral Resources Earth Science Series.

Naipauer, M., Vujovich, G. I., Cingolani, C. A., & McClelland, W. C. (2010). Detrital zircon analysis from the Neoproterozoic-Cambrian sedimentary cover (Cuyania terrane), Sierra de Pie de Palo, Argentina: Evidence of a rift and passive margin system? *Journal of South American Earth Sciences*, *29*(2), 306–326. https://doi.org/10.1016/j.jsames.2009.10.001

Paton, C., Woodhead, J. D., Hellstrom, J. C., Hergt, J. M., Greig, A., & Maas, R. (2010). Improved laser ablation U-Pb zircon geochronology through robust downhole fractionation correction. *Geochemistry, Geophysics, Geosystems*, *11*(3), n/a. https://doi.org/10.1029/2009GC002618

Perez, D. J. (1995). *Estudio geológico del Cordón del Espinacito y regiones adyacentes, provincial de San Juan (Doctoral dissertation)*. Buenos Aires, Argentina: Universidad de Buenos Aires.

Pérez, D. J. (2001). Tectonic and unroofing history of Neogene Manatiales foreland basin deposits, Cordillera Frontal (32°30′S), San Juan Province, Argentina. *Journal of South American Earth Sciences*, *14*(7), 693–705. https://doi.org/10.1016/S0895-9811(01)00071-2

Pérez, D. J., & Ramos, V. A. (1996). Los depósitos sinorogénicos. In M. B. Aguirre-Urreta, P. P. Alvarez, M. Cegarra, E. O. Cristallini, S. M. Kay, G. L. Lo Forte, Pereyra, F. X., D. J. Perez (Eds.) *Direccion Nacional del Servicio Geologico* (24th ed., pp. 387–422). Buenos Aires: Dirección Nacional del Servicio Geológico.

Petrus, J. A., & Kamber, B. S. (2012). VizualAge: A novel approach to laser ablation ICP-MS U-Pb geochronology data reduction. *Geostandards and Geoanalytical Research*, *36*(3), 247–270. https://doi.org/10.1111/j.1751-908X.2012.00158.x

Pinto, L., Alarcón, P., Morton, A., & Naipauer, M. (2018). Geochemistry of heavy minerals and U–Pb detrital zircon geochronology in the Manantiales Basin: Implications for Frontal Cordillera uplift and foreland basin connectivity in the Andes of central Argentina. *Palaeogeography, Palaeoclimatology, Palaeoecology*, *492*, 104–125. https://doi.org/10.1016/j.palaeo.2017.12.017

Piquer, J., Hollings, P., Rivera, O., Cooke, D. R., Baker, M., & Testa, F. (2017). Along-strike segmentation of the Abanico Basin, central Chile: New chronological, geochemical and structural constraints. *Lithos*, *268*, 174–197. https://doi.org/10.1016/j.lithos.2016.10.025

Ragona, D., Anselmi, G., Gonzaléz, P., & Vujovich, G. (1995). *Mapa geológico de la provincia de San Juan. República Argentina*. Buenos Aires, Argentina: Secretaría de Minería, Dirección Nacional Del Servicio Geológico.

Rak, A. J., McQuarrie, N., & Ehlers, T. A. (2017). Kinematics, exhumation, and sedimentation of the north central Andes (Bolivia): An integrated thermochronometer and thermokinematic modeling approach. *Tectonics*, *36*(11), 2524–2554. https://doi.org/10.1002/2016TC004440

Ramos, V. A. (2009). Anatomy and global context of the Andes: Main geologic features and the Andean orogenic cycle. *In Backbone of the Americas: Shallow subduction, plateau uplift, and ridge and terrane collision*, *204*, 31–65. https://doi.org/10.1130/2009.1204(02

Ramos, V. A., Cegarra, M., & Cristallini, E. (1996). Cenozoic tectonics of the High Andes of west-central Argentina (30–36°S latitude). *Tectonophysics*, *259*(1–3), 185–200. https://doi.org/10.1016/0040-1951(95)00064-X

Ramos, V. A., & Folguera, A. (2005). Tectonic evolution of the Andes of Neuquén: Constraints derived from the magmatic arc and foreland deformation. *Geological Society, London, Special Publications*, *252*(1), 15–35. https://doi.org/10.1144/GSL.SP.2005.252.01.02

Ramos, V. A., & Folguera, A. (2009). Andean flat-slab subduction through time. *Geological Society, London, Special Publications*, *327*(1), 31–54. https://doi.org/10.1144/SP327.3

Ramos, V. A., Zapata, T., Cristallini, E. O., & Introcaso, A. (2004). The Andean thrust system—Latitudinal variations in structural styles and orogenic shortening. *AAPG Memoir*, 30–50.

Rapela, C. W., Pankhurst, R. J., Casquet, C., Fanning, C. M., Baldo, E. G., González-Casado, J. M., et al. (2007). The Río de la Plata craton and the assembly of SW Gondwana. *Earth-Science Reviews*, *83*(1-2), 49–82. https://doi.org/10.1016/j.earscirev.2007.03.004

Reiners, P. W., & Brandon, M. T. (2006). Using thermochronology to understand orogenic erosion. *Annual Review of Earth and Planetary Sciences*, *34*, 419–466. https://doi.org/10.1146/annurev.earth.34.031405.125202

Reiners, P. W., & Farley, K. A. (2001). Influence of crystal size on apatite (U-Th)/He thermochronology: An example from the Bighorn Mountains, Wyoming. *Earth and Planetary Science Letters*, *188*(3-4), 413–420. https://doi.org/10.1016/S0012-821X(01)00341-7

Reyna, G., Hoke, G. H., & Dávila, F. M. (2010). *Sedimentation and exhumation of the distal part of the Manantiales Basin: The Chinches Formation, Argentine Precordillera (32° SL), In 18th International Sedimentology Congress, Proceedings* (pp. 1), (). Argentina: Mendoza.

Rivano, S., & Sepúlveda, P. (1991). *Hoja Illapel, Región de Coquimbo (scale 1:250,000, Carta Geológica de Chile 69)*. Santiago, Chile: Servicio Nacional de Geología y Minería.

Rivano, S., Sepúlveda, P., Boric, R., & Espiñeira, D. (1993). *Hoja Quillota y Portillo, V Región (scale 1:250,000, Carta Geológica de Chile 73, 7644)*. Santiago, Chile: Servicio Nacional de Geología y Minería.

Robinson, D. M., & McQuarrie, N. (2012). Pulsed deformation and variable slip rates within the central Himalayan thrust belt. *Lithosphere*, *4*(5), 449–464. https://doi.org/10.1130/L204.1

Rocher, S., & Vallecillo, G. (2014). Mecanismos eruptivos y procesos depositacionales del Grupo Choiyoi en el área de Las Caletas, Cordillera Frontal de San Juan, Argentina. *Andean Geology*, *41*(3), 589–625. https://doi.org/10.5027/andgeoV41n3-a05

Rodríguez, M. P., Charrier, R., Brichau, S., Carretier, S., Farías, M., de Parseval, P., & Ketcham, R. A. (2018). Latitudinal and longitudinal patterns of exhumation in the Andes of north-central Chile. *Tectonics*, *37*(9), 2863–2886. https://doi.org/10.1029/2018TC004997

Ruskin, B. G., Dávila, F. M., Hoke, G. D., Jordan, T. E., Astini, R. A., & Alonso, R. (2011). Stable isotope composition of middle Miocene carbonates of the Frontal Cordillera and Sierras Pampeanas: Did the Paranaense seaway flood western and central Argentina? *Palaeogeography, Palaeoclimatology*. *Palaeoecology*, *308*(3-4), 293–303. https://doi.org/10.1016/j.palaeo.2011.05.033

Ruskin, B. G., & Jordan, T. E. (2007). Climate change across continental sequence boundaries: Paleopedology and lithofacies of Iglesia Basin, northwestern Argentina. *Journal of Sedimentary Research*, *77*(9), 661–679. https://doi.org/10.2110/jsr.2007.069

Sato, A. M., Llambías, E. J., Basei, M. A. S., & Castro, C. E. (2015). Three stages in the Late Paleozoic to Triassic magmatism of southwestern Gondwana, and the relationships with the volcanogenic events in coeval basins. *Journal of South American Earth Sciences.*, *63*, 48–69. https://doi.org/10.1016/j.jsames.2015.07.005

Schellart, W. P. (2017). Andean mountain building and magmatic arc migration driven by subduction-induced whole mantle flow. *Nature Communications.*, *8*(1), 1–13. https://doi.org/10.1038/s41467-017-01847-z

Segemar (2000). *Hoja geologica: 3369-I Cerro Aconcagua (mapa escala 1:250,000)*.

Sernageomin (2003). *Mapa geologico de Chile: version digital* (mapa escala 1:1,000,000) Publicacion Geologia Digital, 4, 25.

Shuster, D. L., Flowers, R. M., & Farley, K. A. (2006). The influence of natural radiation damage on helium diffusion kinetics in apatite. *Earth and Planetary Science Letters*, *249*(3-4), 148–161. https://doi.org/10.1016/j.epsl.2006.07.028

Stockli, D. F., Farley, K. A., & Dumitru, T. A. (2000). Calibration of the apatite (U-Th)/He thermochronometer on anexhumed fault block, White Mountains, California. *Geology, 28*(11), 983-986. https://doi.org/10.1130/0091-7613(2000)28<983:COTAHT>2.0.CO;2

Suriano, J., Mardonez, D., Mahoney, J. B., Mescua, J. F., Giambiagi, L. B., Kimbrough, D., & Lossada, A. (2017). Uplift sequence of the Andes at 30°S: Insights from sedimentology and U/Pb dating of synorogenic deposits. *Journal of South American Earth Sciences*, *75*, 11–34. https://doi.org/10.1016/j.jsames.2017.01.004

Thomson, K. D., Stockli, D. F., Clark, J. D., Puigdefàbregas, C., & Fildani, A. (2017). Detrital zircon (U-Th)/(He-Pb) double-dating constraints on provenance and foreland basin evolution of the Ainsa Basin, south-central Pyrenees, Spain. *Tectonics*, *36*(7), 1352–1375. https://doi.org/10.1002/2017TC004504

Urien, C., Schiefelbein, C., & Zavattieri, A. M. (2009). *The Triassic-Jurassic petroleum system in the SubAndean basins palegeography and geochemistry of the organic rich sequences*, *In 10th Simposio Bolivariano-Exploracion Petrolera en las Cuencas Subandinas*, (). Colombia: Cartagena.

Vallecillo, G., Caballero, M. M., Rocher, S., & Espin, E. (2010). Analisis del Grupo Choiyoi (Permotriásico), Cordillera Frontal de Calingasta, Provincia de San Juan. *Revista de La Asociacion Geologica Argentina*, *66*(1–2), 238–252.

Vergés, J., Ramos, E., Seward, D., Busquets, P., & Colombo, F. (2001). Miocene sedimentary and tectonic evolution of the Andean Precordillera at 31°S, Argentina. *Journal of South American Earth Sciences*, *14*(7), 735–750. https://doi.org/10.1016/S0895-9811(01)00070-0

Vermeesch, P. (2004). How many grains are needed for a provenance study? *Earth and Planetary Science Letters*, *224*(3-4), 441–451. https://doi.org/10.1016/j.epsl.2004.05.037

Vermeesch, P. (2013). Multi-sample comparison of detrital age distributions. *Chemical Geology*, *341*, 140–146. https://doi.org/10.1016/j.chemgeo.2013.01.010

Vernon, A. J., Van Der Beek, P. A., Sinclair, H. D., Persano, C., Foeken, J., & Stuart, F. M. (2009). Variable late Neogene exhumation of the central European Alps: Low-temperature thermochronology from the Aar Massif, Switzerland, and the Lepontine Dome, Italy. *Tectonics*, *28*(5). https://doi.org/10.1029/2008TC002387

Von Gosen, W. (1992). Structural evolution of the Argentine Precordillera: The Río San Juan section. *Journal of Structural Geology*, *14*(6), 643–667.

Willner, A. P., Gerdes, A., & Massonne, H. J. (2008). History of crustal growth and recycling at the Pacific convergent margin of South America at latitudes 29°–36° S revealed by a U-Pb and Lu-Hf isotope study of detrital zircon from late Paleozoic accretionary systems. *Chemical Geology*, *253*(3-4), 114–129. https://doi.org/10.1016/j.chemgeo.2008.04.016

Willner, A. P., Massonne, H. J., Ring, U., Sudo, M., & Thomson, S. N. (2012). P-T evolution and timing of a late Palaeozoic fore-arc system and its heterogeneous Mesozoic overprint in north-central Chile (latitudes 31-32°S). *Geological Magazine*, *149*(2), 177–207. https://doi.org/10.1017/S0016756811000641